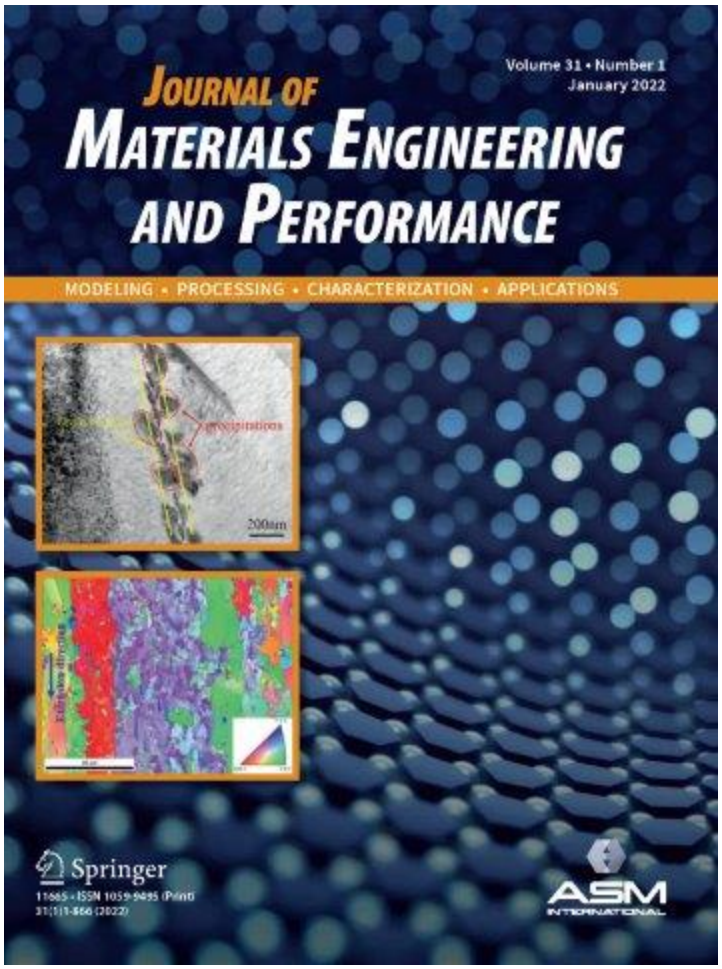

Role of *in situ* Formed Al_3Zr and Al_3Ti Particles on Nucleation of Primary Phase in Cast Al-5 wt. % Cu Alloy

Journal:	*Journal of Materials Engineering and Performance*
Manuscript ID	JMEP-23-02-31205.R2
Manuscript Type:	Technical Article
Date Submitted by the Author:	16-May-2023
Complete List of Authors:	Rakesh, Merugu; Indian Institute of Technology Bombay, Mechanical Engineering SRIVASTAVA, NEERAJ ; Sardar Vallabhbhai National Institute of Technology, Department of Mechanical Engineering; Indian Institute of Technology Bombay, Department of Mechanical Engineering BHAGAVATH, SHISHIRA; University College London, Mechanical Engineering Karagadde, Shyamprasad; Indian Institute of Technology Bombay, Department of Mechanical Engineering

Keywords:	Metal matrix composites (MMC), microstructures, crystallographic orientation relationships, Thermal Analysis, casting

SCHOLARONE™
Manuscripts

Role of in situ Formed (Al_3Zr + Al_3Ti) Particles on Nucleation of Primary Phase in Al-5 wt. % Cu Alloy

Merugu Rakesh[1], Neeraj Srivastava[1, +, *], Shishira Bhagavath[1, #] and Shyamprasad Karagadde[1, *]

[1]Department of Mechanical Engineering, Indian Institute of Technology Bombay, Mumbai 400076 India

[+] Current affiliation: Department of Mechanical Engineering, Sardar Vallabhbhai National Institute of Technology, Surat 395007 India

[#] Current Affiliation: Department of Mechanical Engineering, University College London, WC1E 6BT, UK

*Corresponding author email: s.karagadde@iitb.ac.in, neeraj.s@med.svnit.ac.in

Abstract: Metal matrix composites (MMCs) are known to exhibit improved mechanical properties due to the reinforcing particles, their shape, distribution, and interaction with the matrix. This study investigates the role of *in situ* formed Al_3Zr, Al_3Ti, and a combination of (Al_3Zr+Al_3Ti) particles on the microstructure, crystallographic orientation relationship, and nucleation behaviour of primary Al grains in Al-5 wt.% Cu alloy. The particle dispersion and size were characterized using various microscopy techniques, revealing Al_3Ti and Al_3Zr particles inside and along the grain boundaries, respectively, even though they exhibit similar crystal structures and lattice matching with aluminium. The (Al_3Zr+Al_3Ti) particles were observed to have better distribution in the hybrid composite. Using the edge-to-edge model (E2EM), it was found that the hybrid composite exhibited an increased number of close-packed planes and rows, which facilitated easier nucleation. This was confirmed by a cooling curve analysis, which showed that the hybrid composite required the least undercooling to nucleate grains. Further, a simplified heat transfer analysis indicated that Al_3Ti caused better nucleation per unit particle, likely due to retaining less heat than Al_3Zr. These findings propose a novel mechanism of particle dispersion in the aluminium matrix between the three classes of particles. The study provides valuable insights into the microstructure and crystallographic orientation of *in situ* composites reinforced by multiple particles.

Keywords: Metal matrix composites (MMC); microstructures; crystallographic orientation relationships, thermal analysis; casting.

1. Introduction

Aluminum alloys, are commonly used in the automotive, aeronautical, and aerospace industries for their structural properties (Ref 1–5). Although significant progress has been made in the development of these materials, there is still considerable room for replacing heavier steel components with lighter aluminum alloy parts. Consequently, there is a need for new-age aluminum alloys with high strength-to-weight ratios and excellent mechanical properties (Ref 6–8). One option is the use of metal matrix composites, in which ceramic reinforcing particles are added to the matrix either externally (*ex situ* composites) or generated by chemical reactions with the melt during processing (*in situ* composites) (Ref 9). The usability of *ex situ* composites (Al-X (SiC, TiB_2, TiC, Si_3N_4)) particles as dispersing media often restricted due to the low wettability of the particles in the molten aluminum as well

as the less clean interface between the matrix and particles (Ref 10–14). Composites with *in situ* particles, such as Al-X (TiB_2, TiC, ZrB_2, AIN, B_4C, Al_2O_3, Mg_2Si, Al_3Ti, Al_3Zr), have been found to have good wettability and interface bonding due to the exothermic reactions that occur during the formation of the particles (Ref 15–23). Among these options, Al_3Ti and Al_3Zr particles are particularly promising due to their relatively low density, high melting points, and high Young's modulus (Ref 24,25).

The mechanical properties of *in situ* composites containing aluminides (Al_3Ti, Al_3Zr) are influenced by factors such as particle morphology, distribution, and interface with the matrix. For instance, Liu et al. showed that rod-like Al_3Ti particles in 7075 alloy led to a shift from dendritic to equiaxed microstructure and reduced grain size (Ref 26), while Qin et al. found that changing reaction temperature to 835°C transformed needle-like Al_3Ti particles into finer ones, improving nucleation rate and mechanical properties. Vasanth et al. observed ZrB_2 particles with increased wettability inside the grain of ZrB_2/Al 6061 *in situ* composites, which improved mechanical properties (Ref 27). Dinaharan et al. used stir casting and friction stir processing to study the microstructure of AA 6061/Al_3Ti and AA 6061/Al_3Zr composites, and found clustering of Al_3Ti particles and segregation of needle-shaped Al_3Zr particles near grain boundaries (Ref 28). Hybrid composites containing multiple reinforcing particles, such as B_4C+MoS_2 (Ref 29), Al_4SiC_4+SiC (Ref 30), TiC+TiB_2 (Ref 31), (TiCn+Al_3Tim)/Al (Ref 32), (Al_3Ti+Al_2O_3)/Al (Ref 33), (Al_3Zr+Al_2O_3)/2024Al (Ref 34), (TiB_2+ZrB_2)/Al6061 (Ref 35), (ZrB_2+ZrC)/Al6061 (Ref 36), (Al_2O_3+Al_3Ni)/Al (Ref 37) and various others, have also been developed, but most studies have typically compared the composite with the base alloy. It has been well established that almost all composites are better than the base alloy. However, this work explores the quantitative comparison between two or more composites. Furthermore, the combined effect of multiple particles on microstructure and crystallographic orientation has not been thoroughly investigated. Thus, this research aims to explore the impact of different particles (Al_3Zr, Al_3Ti, and a mixture of Al_3Zr+Al_3Ti) on the nucleation behaviour and microstructure of *in situ* composites.

In addition to the morphology, distribution, and interface between particles and the matrix, crystallographic matching is also crucial for promoting heterogeneous nucleation and improving the mechanical properties of composites (Ref 38). Traditional lattice mismatch calculations were limited to systems with similar crystal structures, which was not viable for most systems (Ref 39). Whereas in the edge-to-edge matching (E2EM) model the crystallographic matching was calculated irrespective of the crystal structure of the system. As a result, the E2EM model was widely used for the calculation of crystallographic matching, especially for Al and Mg alloys (Ref 40). In the E2EM model, the orientation relationships (ORs) between the particles and the metal matrix was determined based on the minimization of interfacial strain energy that in turn minimizes the atomic misfit (Ref 41,42). Based on ORs the corresponding habitat planes were predicted which were the closed-packed (CP) rows/directions as the atomic misfit was minimum. Previously, the mechanism of grain refinement for aluminium with Ti and Zr was studied with the help of crystallography orientation and reported the favourable planes for heterogeneous nucleation (Ref 43). These habitat planes are predicted by the E2EM model for different inoculant particles with the α-Al matrix. Electron Backscatter Diffraction (EBSD) technique was widely used for studying these crystallographic orientations and also, the grain boundaries, types of grain boundaries, texture of material, misorientations, and phase distribution of

For Peer Review

composite (Ref 44). However, there is a paucity of data in the literature on the use of EBSD to study the metal matrix and inoculant particle ORs.

In summary, this research aims to address the knowledge gap in *in situ* composites reinforced by multiple in situ particles in aluminium alloys. The study focuses on the synthesis of *in situ* Al_3Zr/Al-5wt.%Cu, Al_3Ti/Al-5wt.%Cu, (Al_3Zr+Al_3Ti)/Al-5wt.%Cu composites through stir casting, with an emphasis on characterizing the particle dispersion and size using various microscopy techniques. The role of particles on solidification temperatures and undercooling was also analyzed through cooling curve analysis. Furthermore, the crystallographic orientation between particles and the primary phase was studied using the E2EM method.

2. Material and methods

In the preparation of *in situ* composites, Al-5 wt.% Cu alloy was used as the base alloy. The Al-10 wt.% Cu master alloy (Al 89.9 wt. %, Cu 9.5 wt. % and minor elements 0.4 wt.%) was diluted with 99.99% pure aluminium in a stainless-steel crucible using a coreless induction furnace (see supplementary Fig. S1) to prepare the alloy. The Al-5 wt.% Cu alloy was heated to 750 °C to initiate the exothermic reaction after the salt addition. To produce *in situ* composites of Al_3Zr, Al_3Ti, and Al_3Zr + Al_3Ti, 5 wt.% of K_2ZrF_6, 5 wt.% of K_2TiF_6, and (2.5 wt.% K_2ZrF_6 + 2.5 wt.% K_2TiF_6) salts were added to the melt of Al-5 wt.% Cu alloy. The mixture was stirred for 20 minutes at 800 rpm using a REMI-RQ-124A/D stirrer with a graphite stirrer attachment, to achieve the desired particle size and morphology while maintaining the temperature at 750 °C. The Gibbs free energy for the formation of Al_3Ti and Al_3Zr particles at 750 °C is -122.8 kJ/mol and -31.8 kJ/mol respectively (Ref 45). After stirring, the K_3AlF_6 and AlF_3 slags were removed, and the clean melt was poured into a preheated (~400°C) stainless steel mould (30×30×150 mm^3). During solidification, the temperature was measured and recorded using a K-type thermocouple and Pico technology (TC-08) data logger (Ref 46).

Wire electric discharge machining (EDM) was used to cut samples from selected locations in the casting for optical micrography (OM). The specimens were prepared for OM and scanning electron microscopy (SEM) by polishing with wet SiC polishing paper and then with a magnesium oxide powder slurry. The polished samples were etched with a modified Poulton's reagent for grain structure examination. The grain size was measured using a particle analyzer tool in Fiji ImageJ after the images at lower magnification (50 x) were initially segmented using watershed segmentation. Bright-field mode Zeiss Smartzoom 5 digital microscope was used to obtain OM, and 5 micrographs were taken for each sample for measurement of grain size.

The samples are cleaned with ultrasonic cleanser and the dispersion of in situ formed particles was quantified using secondary electron images captured with a Zeiss GEMINI 300 Field Emission Scanning Electron Microscope® (FESEM). Micrographs taken at higher magnification (2000 x) were used to measure the size and shape distribution of the particles in the aluminium matrix. At first, the thresholded micrographs are segmented using simple thresholding in image processing software (Fiji ImageJ). Next, the obtained binary images were used to measure the size and aspect ratio using Analyse tool in the Fiji ImageJ (Ref 47). The crystallographic orientations between the α-Al phase and the composite particles were studied using the EBSD technique (step size = 0.1 μm). For EBSD examination, the samples were polished using 0.04 μm colloidal silica after wet mechanical polishing with different grades of SiC emery papers.

For Peer Review

The samples were electron polished (Tegramin-25 system Inc.) at 20 V for 20 s with a general solution containing 70 ml methanol, 18 ml HNO_3, 6 ml phosphoric acid, and 6 ml perchloric acid. Grain reconstruction and pole figures processing were performed using the Tango-Maps and Mambo-Pole figures platforms in the HKL channel 5® software (Ref 48). Supplementary information 3 contains details of the numerical method utilized for the solution.

3. Results and Discussions:

3.1. Microstructural characterization

Higher magnification optical micrographs (OMs) shown for the as-cast and three composites in Fig. 1 (a-d), indicated that the addition of *in situ* composites led to significant grain refinement. The average grain size for Al-5 wt.% Cu alloy, Al_3Zr/Al, Al_3Ti/Al, and hybrid *in situ* composites found to be 290 µm, 124 µm, 144 µm, and 122 µm, respectively. A closer inspection of the OMs images revealed that in Al_3Ti/Al *in situ* composites, a large fraction of blocky Al_3Ti particles were identified inside the grain (shown in red ovals in Fig. 1(c)), whereas, for Al_3Zr/Al *in situ* composites, the majority of the Al_3Zr particles were found to be segregated along the grain boundaries (highlighted using red arrows in Fig. 1(b)). In the case of *in situ* hybrid composite, most of the particles were present inside the grain (Fig. 1(d)). The SEM micrographs and corresponding EDS analysis further confirmed the presence of blocky Al_3Zr and Al_3Ti particles in Al_3Zr and Al_3Ti *in situ* composites (Fig. 2), while needle-shaped particles (Fig. 2(c) and Fig. 2(f)) in hybrid composites.

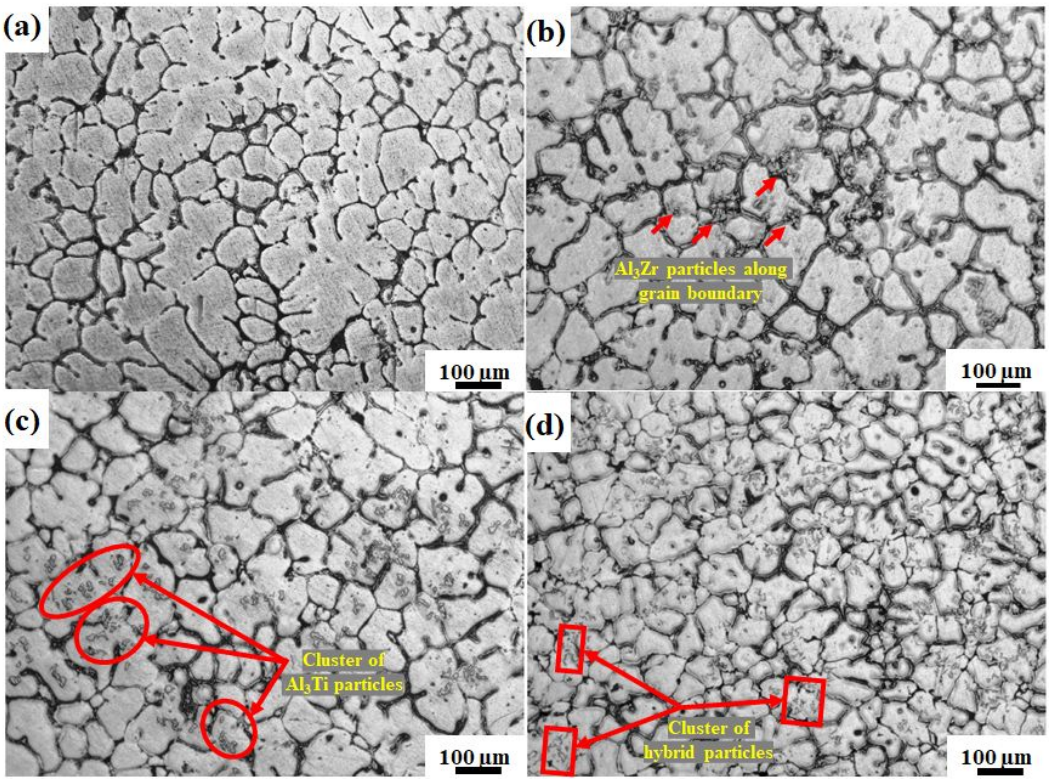

Fig. 1. Optical micrographs of (a) as-cast Al-5 wt.% Cu alloy, (b) Al_3Zr/Al, (c) Al_3Ti/Al, and (d) hybrid *in situ* composites. The red boxes and ovals highlight the particles in the respective composites. Note the contrast of the images is adjusted for better visualization.

The free grain growth model based on the classical heterogeneous nucleation mechanism suggests that the particle size and shape distribution have a major effect on the nucleation potential of the particles for the matrix, during solidification. The particle engulfment/pushing transition is a phenomenon that is controlled by the interfacial energies of the growing front and the particles for a given solidification rate (Ref 49). In the present research, the smaller grain size of Al_3Zr/Al and hybrid composites was due to a greater number of smaller sizes of Al_3Zr and Al_3Ti particles that exert a strong pinning effect (Zener pinning effect (Ref 50)) on grain boundaries in the respective composite. This is confirmed in Fig. 3(a), in which, it is seen that about 95% of particles in hybrid composites are in the range of 1-30 μm^2; while for Al_3Zr/Al and Al_3Ti/Al composites, they were about 70 % and 60% respectively. However, it is to be noted that particle size is not the only criteria, aspect ratio, particle distribution, etc., that will influence the grain refinement as discussed below.

For Peer Review

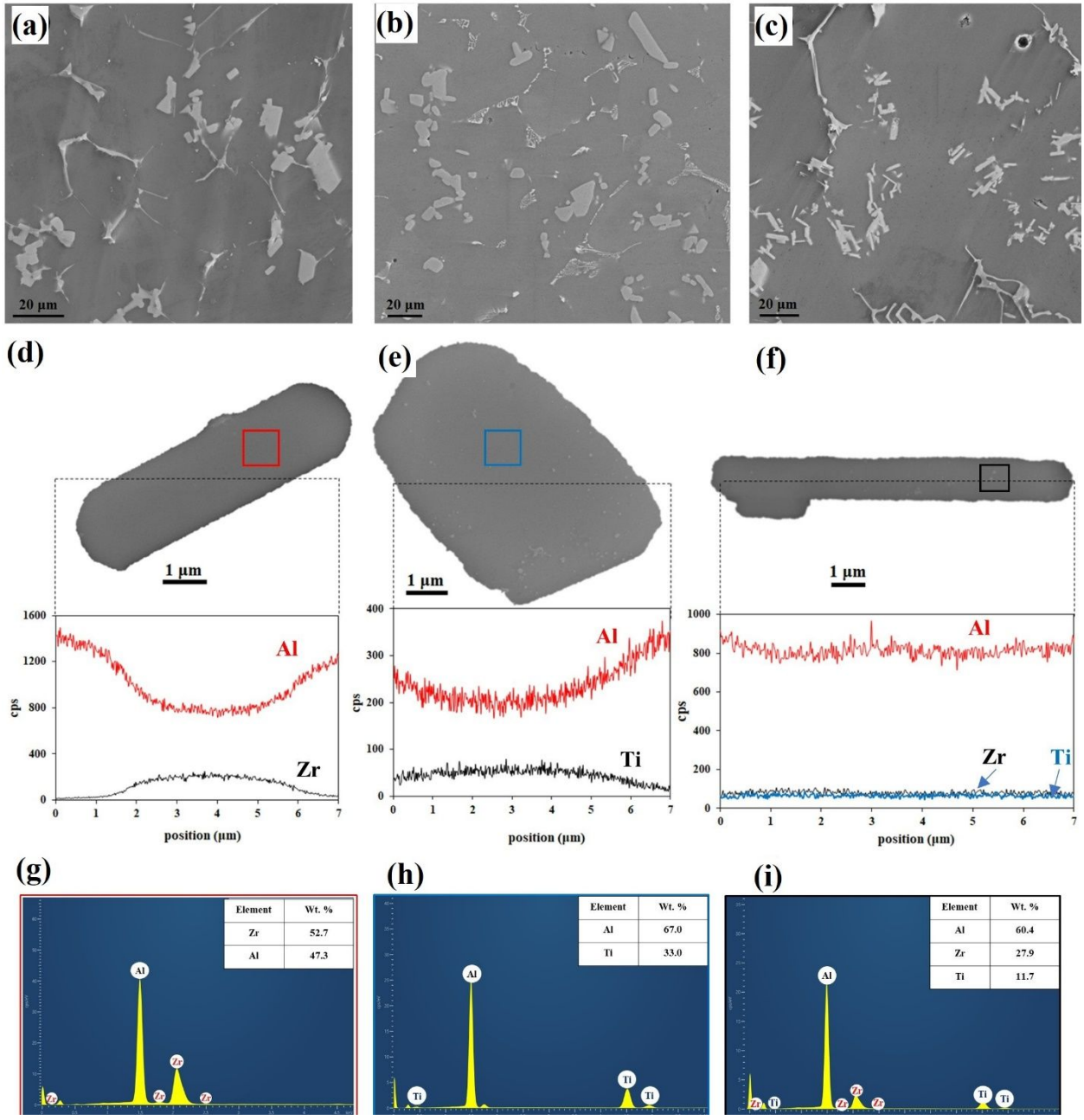

Fig. 2. Higher magnification secondary electron images of (a) Al_3Zr/Al, (b) Al_3Ti/Al, (c) hybrid *in situ* composites, (d-f) corresponding EDS line analysis images of the particles, and (g-i) corresponding EDS spectrum confirming the formation of the *in situ* particles respectively.

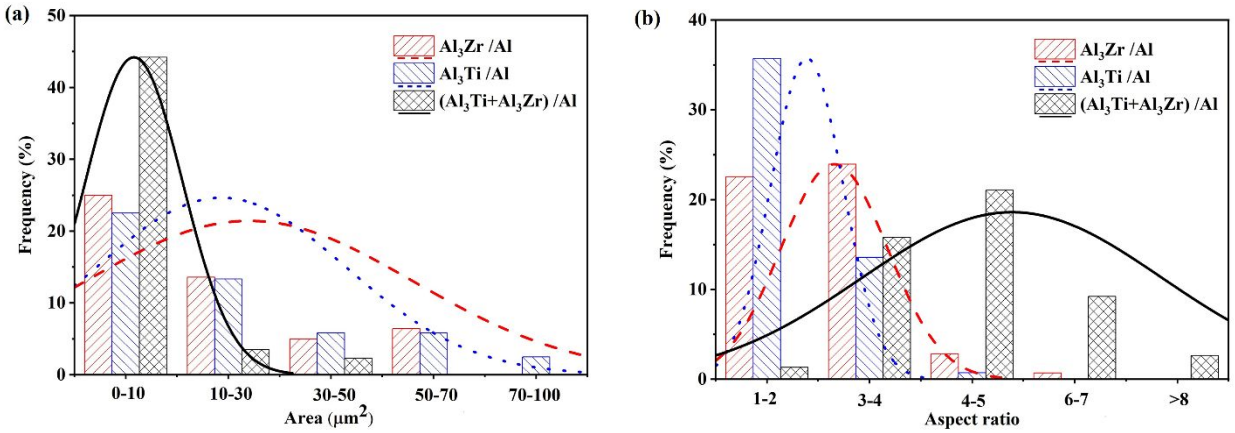

Fig. 3. Particle size distribution and corresponding normal fit of *in situ* formed (a) Al_3Zr, Al_3Ti, and Al_3Zr+Al_3Ti particles compared to the as-cast alloy in their respective composite, (b) Corresponding aspect ratio distribution of the particles.

The particles, which have a smaller aspect ratio, act as heterogeneous nucleation sites for the primary phase and on the other hand, higher aspect ratio size particles considerably restrict the grain growth (Ref 51). In addition, the blocky-shaped particles have a greater number of faces to nucleate the primary grain as compared to the other shapes. Among all these particles (Al_3Zr, Al_3Ti, and Al_3Zr+Al_3Ti particles in their respective composite), it is observed that Al_3Zr and Al_3Ti particles are predominantly blocky, and particles in the hybrid composite are mainly needle-shaped. However, in the case of the Al_3Zr/Al composite, even though the particles are smaller, they do not act as nucleation sites. Whereas, the needle-shaped (Al_3Zr+Al_3Ti) particles with a high aspect ratio act as nucleation sites for α-Al. This observation is explained in the following sections, using the cooling curves, thermal analysis, and the orientation relationships in these composites.

3.2. Cooling curve analysis

The cooling curves (Fig. 4) and their first and second derivatives shed light on the influence of particles on the nucleation of α-Al. An increase in the slope at any point indicates a phase transformation accompanied by a latent heat release. The increment of the derivative indicates the start of the nucleation of the α-Al nonequilibrium Al_2Cu phase (Ref 45). Measured solidification temperatures (see Table 1) show that the undercooling of all the composites is lower than that of as-cast alloy, indicating that the *in situ* particles act as potential heterogeneous nucleation sites for the α-Al phase. Among the composites, the hybrid composite needed the least undercooling (0.93ºC) and Al_3Zr/Al composite the highest (3.74ºC). It is seen that the potency of particles in the hybrid composite is higher followed by Al_3Ti particles than Al_3Zr particles by cooling curve results.

For Peer Review

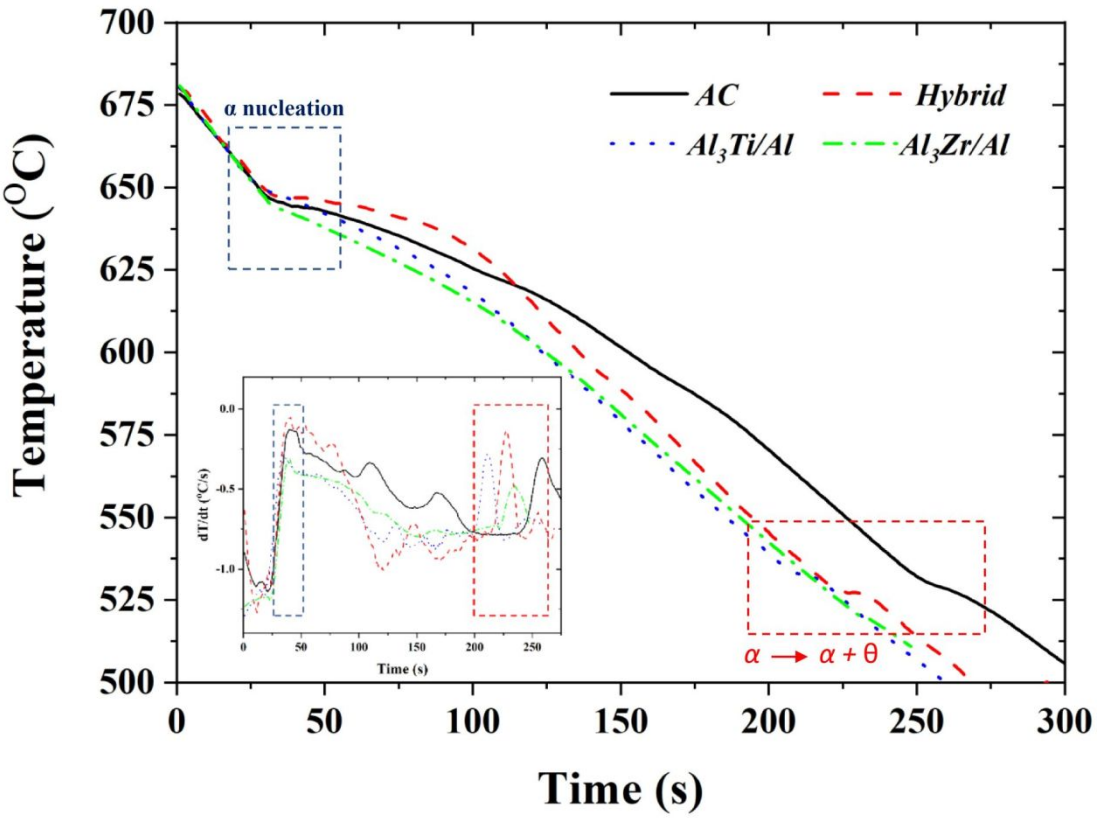

Fig. 4. Cooling curves of as-cast alloy and *in situ* composites. The inset shows the rate of the change of measured temperature of the melt, highlighting the first instance of solidification and eutectic temperature.

Table 1. Thermal parameters extracted from cooling curves (Fig. 4)

Samples	Nucleation temperature (°C) (T_n)	Minimum temperature (°C) (T_m)	Undercooling (°C) $\Delta T = T_n - T_m$
Al-5 wt.% Cu alloy	651.78	646.13	5.64
Al_3Zr/Al composite	647.99	644.21	3.77
Al_3Ti/Al composite	652.22	650.31	1.88
Hybrid *in situ* composite	648.8	647.91	0.93

3.3. Heat transfer analysis

A possible hypothesis for explaining the role of the thermal properties of the particle on the nucleation potency is by investigating the thermal behaviour of the particles in the melt. Thus, a simplified heat transfer analysis between the particle and the surrounding melt is performed (see supplementary information 3). For heat transfer analysis, an axisymmetric system in the radial coordinates was chosen such that the particle was surrounded by the Al-melt, and the heat was constantly removed from the right-side surface. The average particle size is calculated from the micrographs and it was found to be 2.36 μm (Al_3Ti and Al_3Zr). The inside temperature of the Al_3Zr particles was found to be higher than the Al_3Ti particles at any given instant of time as shown in Fig. 5(a). This is because of the

higher thermal capacity of Al_3Zr particles when compared with Al_3Ti particles. Similarly, the enthalpy of the particle with respect to time is shown in Fig. 5(b), indicating that the enthalpy of the Al_3Zr particle is higher than Al_3Ti particles at all times. From the heat transfer analysis, Al_3Zr particles are expected to be more superheated when compared with Al_3Ti particles and a longer time is required for cooling. Despite the blocky and small aspect ratio, Al_3Zr particles might not be a preferred heterogeneous nucleation site for α-Al grains besides the particles were segregated to the grain boundaries, which is the last solidifying region in the melt. Thus, the grain refinement *in situ* Al_3Zr/Al composite is attributed to the restriction of the α-Al phase growth by Al_3Zr particles (Fig. 5(c)). On the other hand, Al_3Ti particles are rapidly cooled compared to that of the Al_3Zr particles during solidification and act as nucleation sites for α-Al grains (Fig. 5(d)). It is to be noted that the interaction between the particles and matrix for the case of hybrid composite is not captured in the model. However, the presence of particles inside the grain and the lowest undercooling suggests that the particles in hybrid composites may have better coherency with α-Al grains which in turn controls the grain growth.

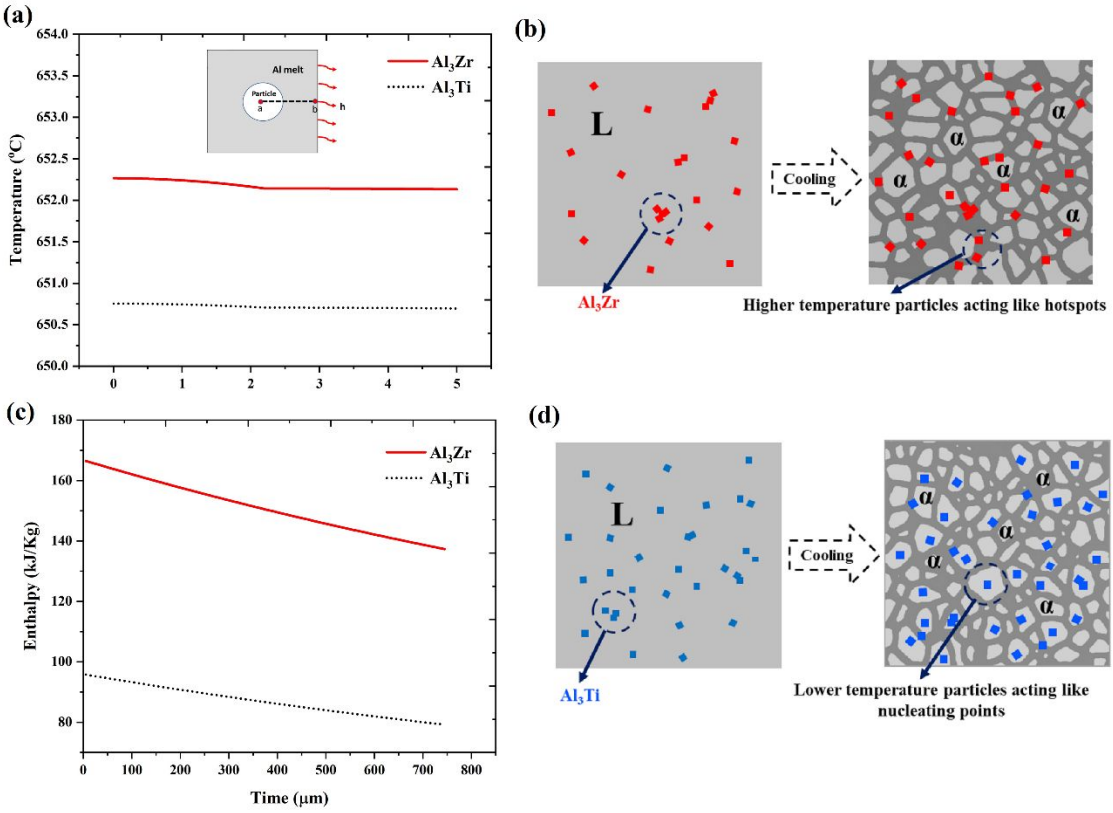

Fig. 5. (a) The variation of the temperature between the two types of particles, and the surrounding melt during solidification is shown in the inset and (c) The enthalpy variation at the interface between particle and the liquid metal for different particles with respect to time, (b) and (d) Schematic of nucleation mechanism of *in situ* Al_3Zr and Al_3Ti composites respectively.

3.4. Orientation relationships

It has been reported that the nucleation potency of particles depends on the lattice matching, with higher lattice matching indicating a greater nucleation potency (Ref 53). For achieving good orientational relationships (ORs), the interatomic misfit (f_r) between matrix and particle should be less than 10% and, the matching rows of atomic arrangement are either zigzag or straight. These matching planes should lie on the closed pack (CP) planes with similar interplanar spacings and, the interplanar spacing misfit value (f_d) should be less than 10% to facilitate easier row matching.

The expression for calculating f_r and f_d is given by equations (1) and (2), respectively:

$$f_r = \frac{|r_M - r_P|}{r_P} \qquad \ldots\ldots\ldots\ldots (1)$$

$$f_d = \frac{|d_M - d_P|}{d_P} \qquad \ldots\ldots\ldots\ldots (2)$$

Here, 'r 'is the inter-atomic distance along the pair of CP rows and the suffixes M and P stand for metal and particles respectively. Similarly, 'd' was the interplanar spacings of the CP planes (Ref 54). The close-pack planes and the rows which were predicted by the E2EM model were experimentally verified with the help of pole figures.

Electron backscatter diffraction (EBSD) analysis was conducted to experimentally analyze the orientation relationships (ORs) between the particles and the matrix. Fig. 6 shows the microstructures and EBSD phase distribution of the three composites, namely Al/Al_3Ti, Al/Al_3Zr, and the hybrid Al, along with elemental mappings. The crystallography ORs between the α-Al phase and Al_3Zr predicted by the E2EM model were experimentally verified by the pole figures presented in Fig. 7. The pole figures of the α-Al phase are Fig. 7(a) and 7(c). The pole figures of Al_3Zr particles are Fig. 7(b) and 7(d). Two kinds of ORs are shown by the pole figures between the α-Al phase and Al_3Zr particles. Fig. 7(a) and 7(b) represent the ORs between the α-Al phase and Al_3Zr particle and Fig. 7(c) and (d) represent the other kind of ORs. Similarly, the crystallographic ORs between the α-Al phase and Al_3Ti predicted by the E2EM model were experimentally verified by the pole figures presented in Fig. 8. The pole figures of the α-Al phase are Fig. 8(a) and 8(c). The pole figures of Al_3Zr particles are Fig. 8(b) and 8(d). Two kinds of ORs are shown by the pole figures between the α-Al phase and Al_3Zr particles. Fig.8(a) and 8(b) represent the ORs between the α-Al phase and Al_3Zr particle and Fig.8(c) and 8(d) represent the other kind of ORs.

The pole figures showed good crystallographic ORs between the particles (Al_3Ti and Al_3Zr) and the α-Al matrix, although fewer pole dots for Al_3Ti were observed even with good ORs, which was attributed to a smaller number of particles in the scan region which was consistent with the Chen and Yen investigation (Ref 43). The crystallographic ORs of the α-Al phase with the hybrid particles exhibited a similar relation as that of individual particles, as shown in Fig. 9. Fig. 9 shows the pole figures of the hybrid composite and the pole figures of Al_3Zr Al_3Ti particles. Fig. 9(a, b), Fig. 9(c, d), Fig. 9(e, f) and Fig. 9(g, h) are the four kinds of ORs between hybrid particles and the α-Al phase. These results provide important insights into the crystallographic orientation of the primary phase in composites reinforced by multiple *in situ* particles.

The theoretical misfit values were calculated from the lattice parameters as reported in Table-2. The close-pack planes are selected according to the E2EM model, and the planes $\{111\}_{Al}$ // $\{112\}_{Al_3Ti}$, $\{111\}_{Al}$ // $\{112\}_{Al_3Ti}$,

For Peer Review

$\{111\}_{Al}$ // $\{114\}_{Al_3Zr}$and $\{220\}_{Al}$ // $\{220\}_{Al_3Zr}$ show the minimum interplanar misfit value of 1.61%, 1.61%, 1.18% and 1.27% respectively. The value of f_r is calculated for the atomic rows that were coupled as straight to straight matching or zigzag-zigzag matching. The corresponding close-pack rows were, $<110>_{Al}$// $<021>_{Al_3Ti}$, $<110>_{Al}$// $<110>_{Al_3Ti}$, $<110>_{Al}$ // $<021>_{Al_3Zr}$ and $<110>_{Al}$ // $<220>_{Al_3Zr}$, with f_r values of 0.73 %, 5.06 %, 1.238 %, and 1.238 % respectively. All the calculated values of f_r and f_d for the selected close-pack planes and rows are well below the 10% misfit criteria. Hence, the predicted planes and rows for both Al_3Ti and Al_3Zr particles with α-Al phase were in good agreement with the EBSD experimental results (Fig. 6 to Fig. 9). In the case of hybrid composite, the combination of Al_3Ti and Al_3Zr particles resulted in an increased number of closed pack planes and corresponding directions (Fig. 9) and pole figures showed four different kinds of crystallographic ORs. As a result, preferable nucleation sites for the α-Al phase increase. Thus, the least undercooling required to nucleate the grains, among all the three *in situ* particles, is for the hybrid particles (Fig. 4 and Table 1) as seen from the cooling curve.

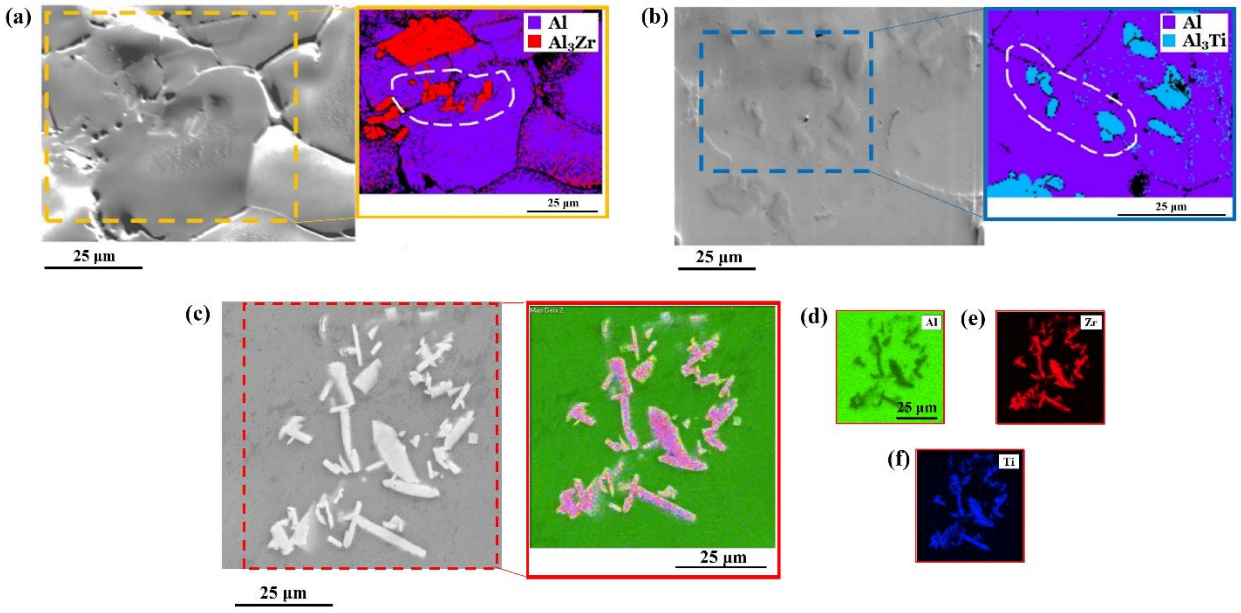

Fig. 6. Microstructure and EBSD phase distribution maps of (a). Al_3Zr/Al, (b). Al_3Ti/Al and (c). Presence of Ti and Zr elements in EDS maps of hybrid composite and (d)-(f) EDS elemental mapping of aluminium, zirconium, and titanium respectively.

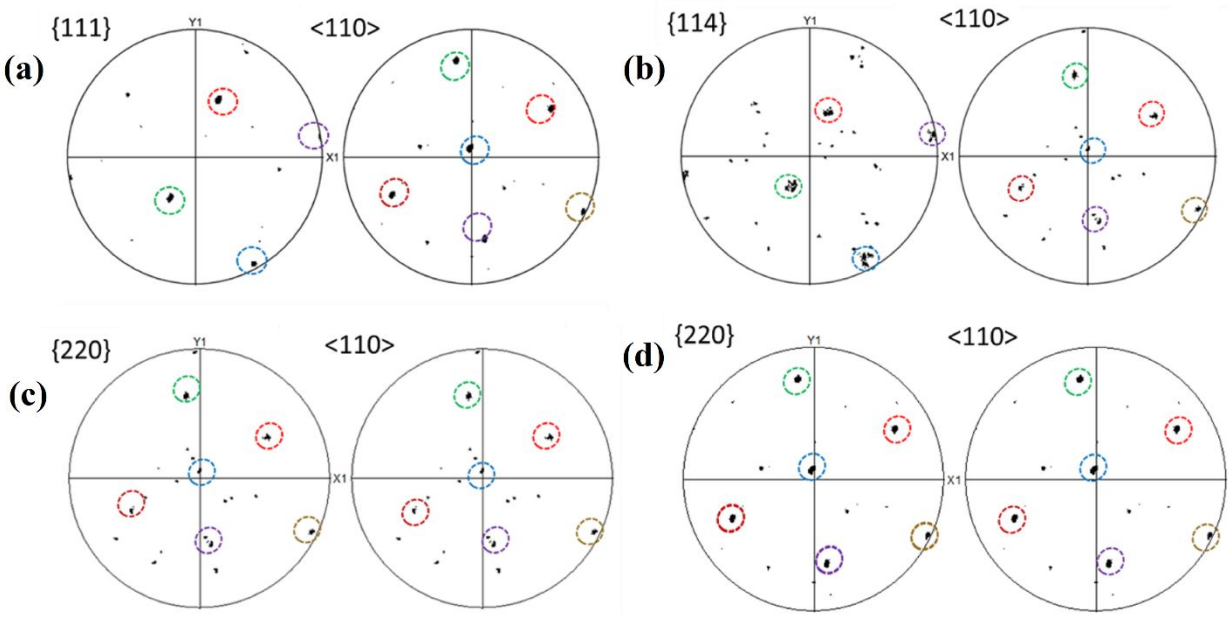

Fig. 7. Pole figures of *in situ* Al_3Zr/Al composites, (a) and (c) for α-Al phase, (b) and (d) for Al_3Zr phase (The dotted circles represent the pole dots of α-Al and Al_3Zr particles).

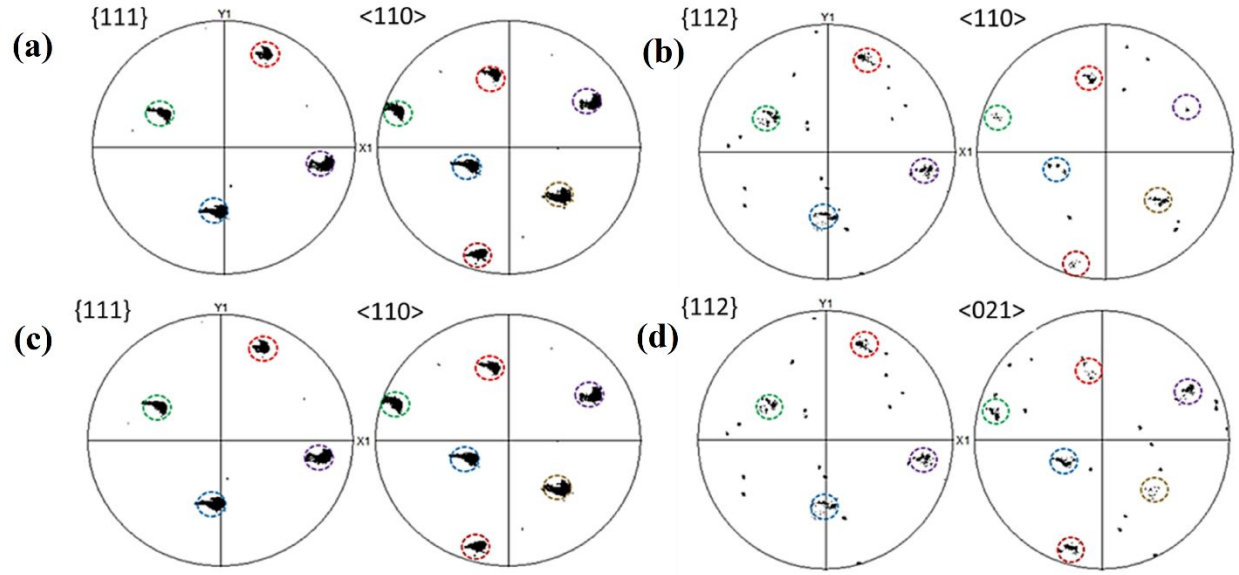

Fig. 8. Pole figures of *in situ* Al_3Ti/Al composites, (a) and (c) for α-Al phase, (b) and (d) for Al_3Ti phase (The dotted circles represent the pole dots of α-Al and Al_3Ti particles).

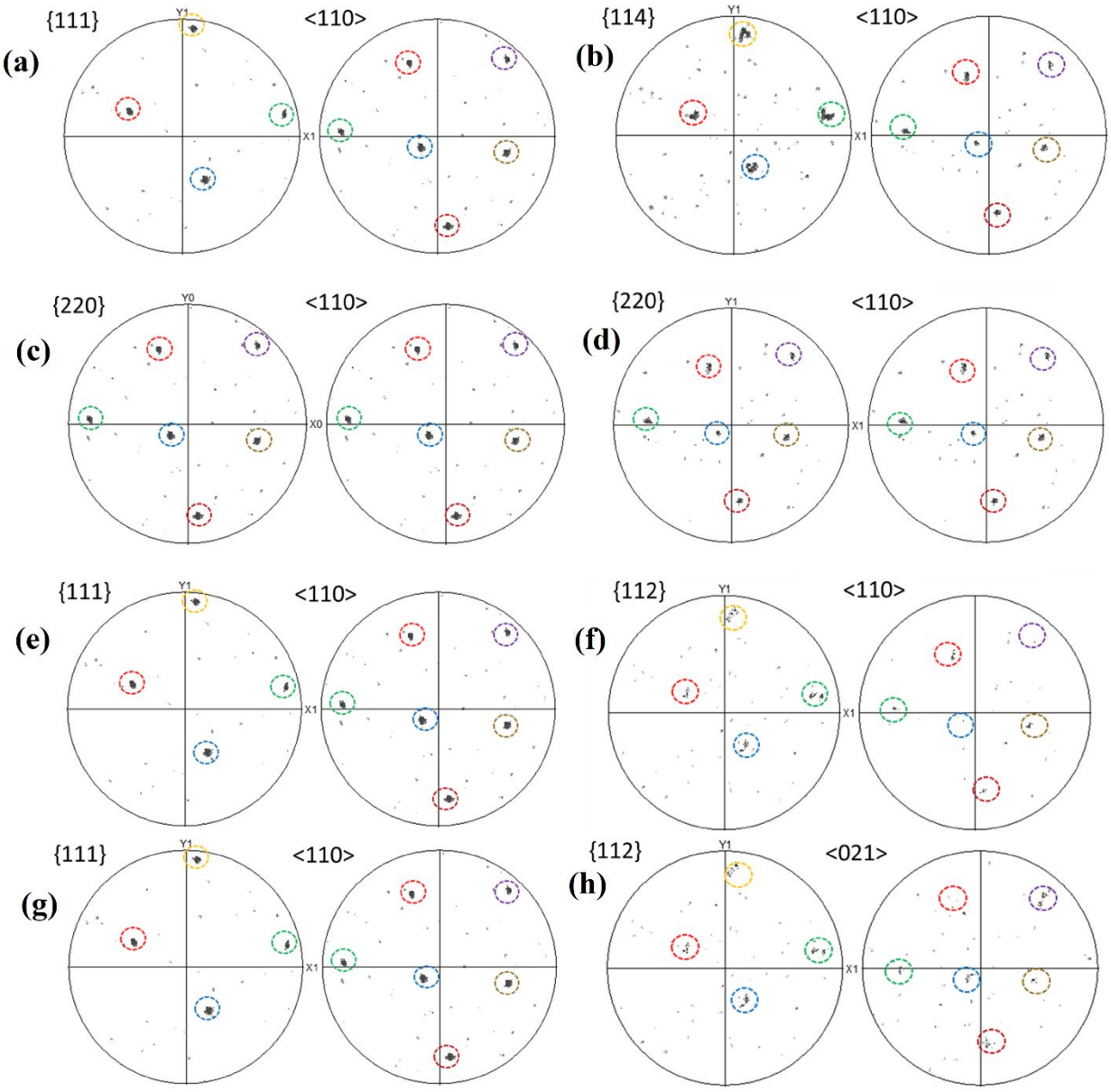

Fig. 9. Pole figures of *in situ* hybrid composite, (a), (c), (e), (g) α-Al phase, (b) and (d) for Al_3Zr phase, (f) and (h) for Al_3Ti phase (The dotted circles represent the pole dots of α-Al, Al_3Ti and Al_3Zr particles).

Table 2. E2EM model predicted crystallographic orientation relationships between Al, Al_3Ti and Al_3Zr particle

Material	Lattice Parameter (nm)			CP Planes	f_d %	CP Directions	f_r %
	a	b	c				
Al	0.4049	-	-	-	-	-	-
Al_3Ti	0.3854	-	0.8584	$\{111\}_{Al}//\{112\}_{Al_3Ti}$	1.61	$<110>_{Al}//<021>_{Al_3Ti}$	0.73
				$\{111\}_{Al}//\{112\}_{Al_3Ti}$	1.61	$<110>_{Al}//<110>_{Al_3Ti}$	5.06
Al_3Zr	0.3999	-	1.7283	$\{111\}_{Al}//\{114\}_{Al_3Zr}$	1.18	$<110>_{Al}//<021>_{Al_3Zr}$	1.238
				$\{220\}_{Al}//\{220\}_{Al_3Zr}$	1.27	$<110>_{Al}//<220>_{Al_3Zr}$	1.238

The results of this research recommend that along with the coherency of particles with the substrate, the thermal properties of particles were also essential to understand the nucleation of the primary phase. The presence of clusters of particles in each composite suggested that the application of mechanical stirring is unable to uniformly disperse the *in situ* particles in the matrix in the present study. Further, EBSD is used for studying the crystal orientation and observing comparable results for the particles and the matrix materials.

3. Conclusions:

Reinforced *in situ* formed Al_3Zr, Al_3Ti, and hybrid particles in Al-5 wt.% Cu alloy were investigated for the efficacy of nucleation and grain refinement.

- From the cooling curve analysis, it was found that the least amount of undercooling is required in the case of a hybrid composite and consequently, the minimum grain size (122 μm) was achieved in the hybrid composite.
- One-dimensional heat transfer analysis between the particles and the surrounding melt showed that Al_3Zr particles cooled at a slower rate when compared with the Al_3Ti particles. Thus, they were not a preferential site for nucleation.
- The grain refinement of the hybrid composite was analyzed by studying the crystallographic ORs between the Al phase and the particles (Al_3Ti, Al_3Zr, hybrid) as per the E2EM model were experimentally verified and observed a good orientation matching.

Acknowledgements:

Authors acknowledge the financial support from the Department of Science and Technology's (DST) Advanced Manufacturing Technologies (AMT), grant reference DST/AMT/2017/141/G and Microstructural Mechanics and Micro Forming (MMMF) lab, IIT Bombay for the use of EBSD facility. Merugu Rakesh wants to

For Peer Review

thank the Ministry of Education, Govt. India for Prime Minister Research Fellow Grant. The authors want to thank Prof. Asim Tewari (Faculty, IIT Bombay) and G. S. Abhishek (PhD scholar, IIT Bombay) for fruitful discussions.

References:

1. C.F. Lin, T.H. Chen, L. Tsai, T.H. Hsieh, W.C. Su, and I.H. Wang, Investigation into Quasi-Static and Dynamic Tensile Mechanical Properties of Aluminium–Scandium Alloy, *Mater. Sci. Technol. (United Kingdom)*, Routledge, 2020, **36**(17), p 1820–1828.
2. M. Balakrishnan, I. Dinaharan, R. Palanivel, and R. Sathiskumar, Influence of Friction Stir Processing on Microstructure and Tensile Behavior of AA6061/Al3Zr Cast Aluminum Matrix Composites, *J. Manuf. Process.*, Elsevier, 2019, **38**(September 2018), p 148–157.
3. M. Malaki, W. Xu, A.K. Kasar, P.L. Menezes, H. Dieringa, R.S. Varma, and M. Gupta, "Advanced Metal Matrix Nanocomposites," *Metals*, 2019.
4. M. Song, D. Xiao, and F. Zhang, Effect of Ce on the Thermal Stability of the Ω Phase in an Al-Cu-Mg-Ag Alloy, *Rare Met.*, 2009, **28**(2), p 156–159.
5. C.Y. Liu, G.B. Teng, Z.Y. Ma, L.L. Wei, W.B. Zhou, H.F. Huang, and H.Q. Qi, Mechanical Properties and Thermal Stability of 7055 Al Alloy by Minor Sc Addition, *Rare Met.*, Nonferrous Metals Society of China, 2020, **39**(6), p 725–732, doi:10.1007/s12598-018-1190-z.
6. M.R. Gazizov, A.O. Boev, C.D. Marioara, S.J. Andersen, R. Holmestad, R.O. Kaibyshev, D.A. Aksyonov, and V.S. Krasnikov, The Unique Hybrid Precipitate in a Peak-Aged Al-Cu-Mg-Ag Alloy, *Scr. Mater.*, Elsevier Ltd, 2021, **194**, p 113669.
7. M.N. Patel, D. Qiu, G. Wang, M.A. Gibson, A. Prasad, D.H. StJohn, and M.A. Easton, Understanding the Refinement of Grains in Laser Surface Remelted Al–Cu Alloys, *Scr. Mater.*, Elsevier Ltd, 2020, **178**, p 447–451.
8. N. Srivastava and G.P. Chaudhari, Grain Refinement in Ultrasonicated Binary Aluminium Alloys, *J. Cryst. Growth*, Elsevier B.V., 2020, **532**(October 2019), p 125415, doi:10.1016/j.jcrysgro.2019.125415.
9. Y.H. Song, M. Tane, T. Ide, Y. Seimiya, B.Y. Hur, and H. Nakajima, Fabrication of Al-3.7 PCT Si-0.18 PCT MG Foam Strengthened by Aln Particle Dispersion and Its Compressive Properties, *Metall. Mater. Trans. A Phys. Metall. Mater. Sci.*, 2010, **41**(8), p 2104–2111.
10. G. Gautam and A. Mohan, Effect of ZrB2 Particles on the Microstructure and Mechanical Properties of Hybrid (ZrB2 + Al3Zr)/AA5052 Insitu Composites, *J. Alloys Compd.*, 2015, **649**, p 174–183.
11. G.B.V. Kumar, P.P. Panigrahy, S. Nithika, R. Pramod, and C.S.P. Rao, Assessment of Mechanical and Tribological Characteristics of Silicon Nitride Reinforced Aluminum Metal Matrix Composites, *Compos. Part B Eng.*, Elsevier Ltd, 2019, **175**(June), p 107138, doi:10.1016/j.compositesb.2019.107138.
12. M. Malaki, A.F. Tehrani, B. Niroumand, and M. Gupta, Wettability in Metal Matrix Composites, *Metals (Basel).*, 2021, **11**(7), p 1–24.
13. J. Suthar and K.M. Patel, Processing Issues, Machining, and Applications of Aluminum Metal Matrix Composites, *Mater. Manuf. Process.*, Taylor & Francis, 2018, **33**(5), p 499–527,

For Peer Review

doi:10.1080/10426914.2017.1401713.

14. H. Dai and X. Liu, Effects of Individual and Combined Additions of Phosphorus, Boron and Cerium on Primary and Eutectic Silicon in an Al-30Si Alloy, *Rare Met.*, 2009, **28**(6), p 651–655.
15. S.L. Pramod, S.R. Bakshi, and B.S. Murty, Aluminum-Based Cast In Situ Composites: A Review, *J. Mater. Eng. Perform.*, Springer US, 2015, **24**(6), p 2185–2207, doi:10.1007/s11665-015-1424-2.
16. Z. Liu, N. Cheng, Q. Zheng, J. Wu, Q. Han, Z. Huang, J. Xing, Y. Li, and Y. Gao, Processing and Tensile Properties of A356 Composites Containing in Situ Small-Sized Al3Ti Particulates, *Mater. Sci. Eng. A*, Elsevier B.V., 2018, **710**(September 2017), p 392–399.
17. V.A. Popov, M. Burghammer, M. Rosenthal, and A. Kotov, In Situ Synthesis of TiC Nano-Reinforcements in Aluminum Matrix Composites during Mechanical Alloying, *Compos. Part B Eng.*, Elsevier, 2018, **145**(January), p 57–61, doi:10.1016/j.compositesb.2018.02.023.
18. N. Srivastava, S. Bhagavath, and S. Karagadde, Effect of in Situ Al3Zr Particles on Controlling the Pore Morphology of Al6061 Alloy Foams, *Mater. Today Commun.*, Elsevier Ltd, 2021, **26**(October), p 101853, doi:10.1016/j.mtcomm.2020.101853.
19. Q. Hu, H. Zhao, and F. Li, Effects of Manufacturing Processes on Microstructure and Properties of Al/A356–B4C Composites, *Mater. Manuf. Process.*, 2016, 2016, **31**(10), p 1292–1300, doi:10.1080/10426914.2016.1151049.
20. Y. Zeng, D. Himmler, P. Randelzhofer, and C. Körner, In Situ Al3Ti/Al Composites Fabricated by High Shear Technology: Microstructure and Mechanical Properties, *Mater. Sci. Technol. (United Kingdom)*, Routledge, 2019, **35**(18), p 2294–2303.
21. Y. Tian, Y. An, C. Wei, B. Xi, S. Xiong, J. Feng, and Y. Qian, Flexible and Free-Standing Ti3C2Tx MXene@Zn Paper for Dendrite-Free Aqueous Zinc Metal Batteries and Nonaqueous Lithium Metal Batteries, *ACS Nano*, 2019, **13**(10), p 11676–11685.
22. Y. Wu, R. Yang, S. Li, Y. Ma, S. Gong, and Y. Han, Surface Recrystallization of a Ni3Al Based Single Crystal Superalloy at Different Annealing Temperature and Blasting Pressure, *Rare Met.*, 2012, **31**(3), p 209–214.
23. M. Zhu, G. Yang, L. Yao, S. Cheng, and Y. Zhou, Influence of Al-Ti-B Addition on the Microstructure and Mechanical Properties of A356 Alloys, *Rare Met.*, 2009, **28**(2), p 181–186.
24. H. Li, K. Wang, G. Xu, H. Jiang, Q. Wang, and W. Ding, "Nanoparticle-Induced Growth Behavior of Primary α-Mg in AZ91 Alloys," *Materials and Design*, 2020.
25. Z. Liu, M. Rakita, X. Wang, W. Xu, and Q. Han, In Situ Formed Al3 Ti Particles in Al Alloy Matrix and Their Effects on the Microstructure and Mechanical Properties of 7075 Alloy, *J. Mater. Res.*, 2014, **29**(12), p 1354–1361.
26. J. Qin, G. Chen, X. Ji, X. Song, N. Hu, F. Han, and Z. Du, Effect of Reaction Temperature on the Microstructures and Mechanical Properties of High-Intensity Ultrasonic Assisted in-Situ Al3Ti/2024 Al Composites, *J. Alloys Compd.*, Elsevier B.V, 2016, **666**, p 58–64, doi:10.1016/j.jallcom.2016.01.121.
27. R.V. Kumar, R. Keshavamurthy, and C.S. Perugu, Microstructure and Mechanical Behaviour of Al6061-

For Peer Review

ZrB2 In-Situ Metal Matrix Composites, *IOP Conf. Ser. Mater. Sci. Eng.*, 2016, **149**(1).

28. I. Dinaharan, G. Ashok Kumar, S.J. Vijay, and N. Murugan, Development of Al3Ti and Al3Zr Intermetallic Particulate Reinforced Aluminum Alloy AA6061 in Situ Composites Using Friction Stir Processing, *Mater. Des.*, Elsevier Ltd, 2014, **63**, p 213–222, doi:10.1016/j.matdes.2014.06.008.
29. S. Liu, Y. Wang, T. Muthuramalingam, and G. Anbuchezhiyan, Effect of B4C and MOS2 Reinforcement on Micro Structure and Wear Properties of Aluminum Hybrid Composite for Automotive Applications, *Compos. Part B Eng.*, Elsevier Ltd, 2019, **176**(July), p 107329, doi:10.1016/j.compositesb.2019.107329.
30. B. Kumar Show, D. Kumar Mondal, K. Biswas, and J. Maity, Development of a Novel 6351 Al-(Al4SiC4+SiC) Hybrid Composite with Enhanced Mechanical Properties, *Mater. Sci. Eng. A*, Elsevier, 2013, **579**, p 136–149, doi:10.1016/j.msea.2013.04.105.
31. H.Y. Yang, Z. Wang, L.Y. Chen, S.L. Shu, F. Qiu, and L.C. Zhang, Interface Formation and Bonding Control in High-Volume-Fraction (TiC+TiB2)/Al Composites and Their Roles in Enhancing Properties, *Compos. Part B Eng.*, Elsevier Ltd, 2021, **209**(January), p 108605, doi:10.1016/j.compositesb.2021.108605.
32. Q. Li, F. Qiu, Y.Y. Gao, B.X. Dong, S.L. Shu, M.M. Lv, H.Y. Yang, Q.L. Zhao, and Q.C. Jiang, Microstructure Refinement and Strengthening Mechanisms of Bimodal-Sized and Dual-Phased (TiCn-Al3Tim)/Al Hybrid Composites Assisted Ultrasonic Vibration, *J. Alloys Compd.*, 2019, **788**, p 1309–1321.
33. M.S. Ahmadvand, A. Azarniya, and H.R. Madaah Hosseini, Thermomechanical Synthesis of Hybrid In-Situ Al-(Al3Ti+Al2O3) Composites through Nanoscale Al-Al2TiO5 Reactive System, *J. Alloys Compd.*, Elsevier B.V, 2019, **789**, p 493–505.
34. B. Kaveendran, G.S. Wang, L.J. Huang, L. Geng, and H.X. Peng, In Situ (Al3Zr + Al2O3np)/2024Al Metal Matrix Composite with Novel Reinforcement Distributions Fabricated by Reaction Hot Pressing, *J. Alloys Compd.*, Elsevier B.V., 2013, **581**, p 16–22.
35. A. Mahamani and V. V. Anantha Chakravarthy, Investigation on Laser Drilling of AA6061-TiB2/ZrB2 in Situ Composites, *Mater. Manuf. Process.*, 2017, **32**(15), p 1700–1706.
36. S. Rajesh Ruban, K. Leo Dev Wins, J. David Raja Selvam, and R.S. Rai, Experimental Investigation and Characterization of in Situ Synthesized Sub Micron ZrB2-ZrC Particles Reinforced Hybrid AA6061 Aluminium Composite, *Mater. Res. Express*, IOP Publishing, 2019, **6**(10).
37. A.R. Najarian, R. Emadi, and M. Hamzeh, Fabrication of As-Cast Al Matrix Composite Reinforced by Al2O3/Al3Ni Hybrid Particles via in-Situ Reaction and Evaluation of Its Mechanical Properties, *Mater. Sci. Eng. B*, Elsevier, 2018, **231**, p 57–65.
38. T.E. Quested, Understanding Mechanisms of Grain Refinement of Aluminium Alloys by Inoculation, *Mater. Sci. Technol.*, 2004, **20**(11), p 1357–1369.
39. Bruce L. Bramfitt, The Effect of Carbide and Nitride Additions on the Heterogeneous Nucleation Behavior of Liquid Iron, *Metall. Trans.*, 1970, **1**(7), p 1987–1995.
40. F. Wang, D. Qiu, Z.L. Liu, J. Taylor, M. Easton, and M.X. Zhang, Crystallographic Study of Al3Zr and Al3Nb as Grain Refiners for Al Alloys, *Trans. Nonferrous Met. Soc. China (English Ed.*, 2014, **24**(7), p 2034–2040.

For Peer Review

41. M.X. Zhang and P.M. Kelly, Edge-to-Edge Matching and Its Applications: Part I. Application to the Simple HCP/BCC System, *Acta Mater.*, 2005, **53**(4), p 1073–1084.
42. M.X. Zhang and P.M. Kelly, Edge-to-Edge Matching and Its Applications: Part II. Application to Mg-Al, Mg-Y and Mg-Mn Alloys, *Acta Mater.*, 2005, **53**(4), p 1085–1096.
43. Z. Chen and K. Yan, Grain Refinement of Commercially Pure Aluminum with Addition of Ti and Zr Elements Based on Crystallography Orientation, *Sci. Rep.*, Nature Publishing Group UK, 2020, **10**(1), p 1–8, doi:10.1038/s41598-020-73799-2.
44. S. Otarawanna, C.M. Gourlay, H.I. Laukli, and A.K. Dahle, Agglomeration and Bending of Equiaxed Crystals during Solidification of Hypoeutectic Al and Mg Alloys, *Acta Mater.*, Acta Materialia Inc., 2010, **58**(1), p 261–271, doi:10.1016/j.actamat.2009.09.002.
45. V. Kumar, A. Srivastava, and S. Karagadde, Role of Microstructure and Composition on Natural Convection during Ternary Alloy Solidification, *J. Fluid Mech.*, 2021, **913**, p 1–29.
46. J. Schindelin, I. Arganda-Carreras, E. Frise, V. Kaynig, M. Longair, T. Pietzsch, S. Preibisch, C. Rueden, S. Saalfeld, B. Schmid, J.Y. Tinevez, D.J. White, V. Hartenstein, K. Eliceiri, P. Tomancak, and A. Cardona, Fiji: An Open-Source Platform for Biological-Image Analysis, *Nat. Methods*, 2012, **9**(7), p 676–682.
47. S. Yotte, D. Breysse, J. Riss, and S. Ghosh, Cluster Characterisation in a Metal Matrix Composite, *Mater. Charact.*, 2001, **46**(2–3), p 211–219.
48. A. Ranjan, J.S. Jha, and S.K. Mishra, The Role of Microstructure Inhomogeneity in Ti-6Al-4V Forging on Fracture Toughness Behavior, *J. Mater. Eng. Perform.*, Springer US, 2022, (Ref 16), doi:10.1007/s11665-022-06862-w.
49. A.L. Greer, J.H. Perepezko, F. Franks, B. Cantor, and R.W. Cahn, Grain Refinement of Alloys by Inoculation of Melts, *Philos. Trans. R. Soc. A Math. Phys. Eng. Sci.*, 2003, **361**(1804), p 479–495.
50. K.R. Ramkumar and S. Natarajan, Tensile Properties and Strengthening Effects of Al 3003 Alloy Weldment Reinforced with TiO2 Nanoparticles, *Compos. Part B Eng.*, Elsevier Ltd, 2019, **175**(June), p 107159, doi:10.1016/j.compositesb.2019.107159.
51. Z.L. Chao, L.C. Zhang, L.T. Jiang, J. Qiao, Z.G. Xu, H.T. Chi, and G.H. Wu, Design , Microstructure and High Temperature Properties of in-Situ Al3Ti and Nano-Al2O3 Reinforced 2024Al Matrix Composites from Al-TiO2 System, *J. Alloys Compd.*, 2019, **775**, p 290–297.
52. K.M. Amin and N.A. Mufti, Investigating Cooling Curve Profile and Microstructure of a Squeeze Cast Al-4%Cu Alloy, *J. Mater. Process. Technol.*, Elsevier B.V., 2012, **212**(8), p 1631–1639, doi:10.1016/j.jmatprotec.2012.02.017.
53. R. Gupta and B.S.S. Daniel, "Impression Creep Behaviour of Ultrasonically Processed In-Situ Al3Ti Reinforced Aluminium Composite," *Materials Science and Engineering A*, 2018, p 257–266.
54. D. Qiu, J.A. Taylor, and M.X. Zhang, Understanding the Co-Poisoning Effect of Zr and Ti on the Grain Refinement of Cast Aluminum Alloys, *Metall. Mater. Trans. A Phys. Metall. Mater. Sci.*, 2010, **41**(13), p 3412–3421.

For Peer Review

Figure captions:

Fig. 1. Optical micrographs of (a) as-cast Al-5 wt.% Cu alloy, (b) Al_3Zr/Al, (c) Al_3Ti/Al, and (d) hybrid *in situ* composites. The red boxes and ovals highlight the particles in the respective composites. Note the contrast of the images is adjusted for better visualization.

Fig. 2. Higher magnification secondary electron images of (a) Al_3Zr/Al, (b) Al_3Ti/Al, (c) hybrid *in situ* composites, (d-f) corresponding EDS line analysis images of the particles, and (g-i) corresponding EDS spectrum confirming the formation of the *in situ* particles respectively.

Fig. 3. Particle size distribution and corresponding normal fit of *in situ* formed (a) Al_3Zr, Al_3Ti, and Al_3Zr+Al_3Ti particles compared to the as-cast alloy in their respective composite, (b) Corresponding aspect ratio distribution of the particles.

Fig. 4. Cooling curves of as-cast alloy and *in situ* composites. The inset shows the rate of the change of measured temperature of the melt, highlighting the first instance of solidification and eutectic temperature.

Fig. 5. (a) The variation of the temperature between the two types of particles, and the surrounding melt during solidification is shown in the inset and (c) The enthalpy variation at the interface between particle and the liquid metal for different particles with respect to time, (b) and (d) Schematic of nucleation mechanism of *in situ* Al_3Zr and Al_3Ti composites respectively.

Fig. 6. Microstructure and EBSD phase distribution maps of (a). Al_3Zr/Al, (b). Al_3Ti/Al and (c). Presence of Ti and Zr elements in EDS maps of hybrid composite and (d)-(f) EDS elemental mapping of aluminium, zirconium, and titanium respectively.

Fig. 7. Pole figures of *in situ* Al_3Zr/Al composites, (a) and (c) for α-Al phase, (b) and (d) for Al_3Zr phase (The dotted circles represent the pole dots of α-Al and Al_3Zr particles).

Fig. 8. Pole figures of *in situ* Al_3Ti/Al composites, (a) and (c) for α-Al phase, (b) and (d) for Al_3Ti phase (The dotted circles represent the pole dots of α-Al and Al_3Ti particles).

Fig. 9. Pole figures of *in situ* hybrid composite, (a), (c), (e), (g) α-Al phase, (b) and (d) for Al_3Zr phase, (f) and (h) for Al_3Ti phase (The dotted circles represent the pole dots of α-Al, Al_3Ti and Al_3Zr particles).

For Peer Review

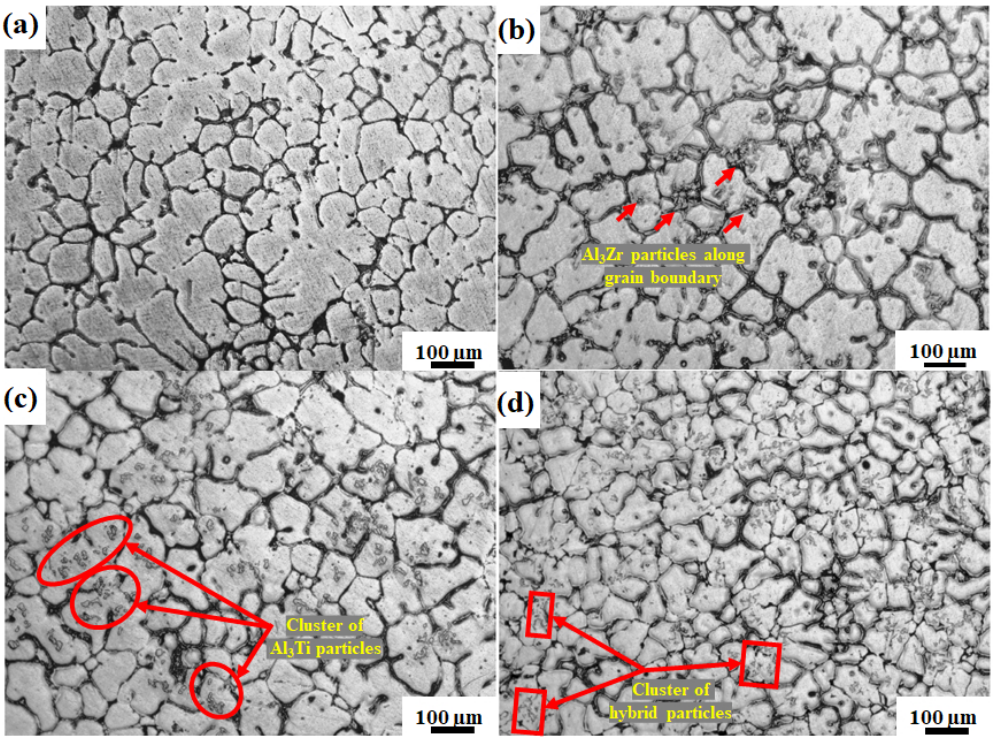

Fig. 1. Optical micrographs of (a) as-cast Al-5 wt.% Cu alloy, (b) Al_3Zr/Al, (c) Al_3Ti/Al, and (d) hybrid *in situ* composites. The red boxes and ovals highlight the particles in the respective composites. Note the contrast of the images is adjusted for better visualization.

73x54mm (300 x 300 DPI)

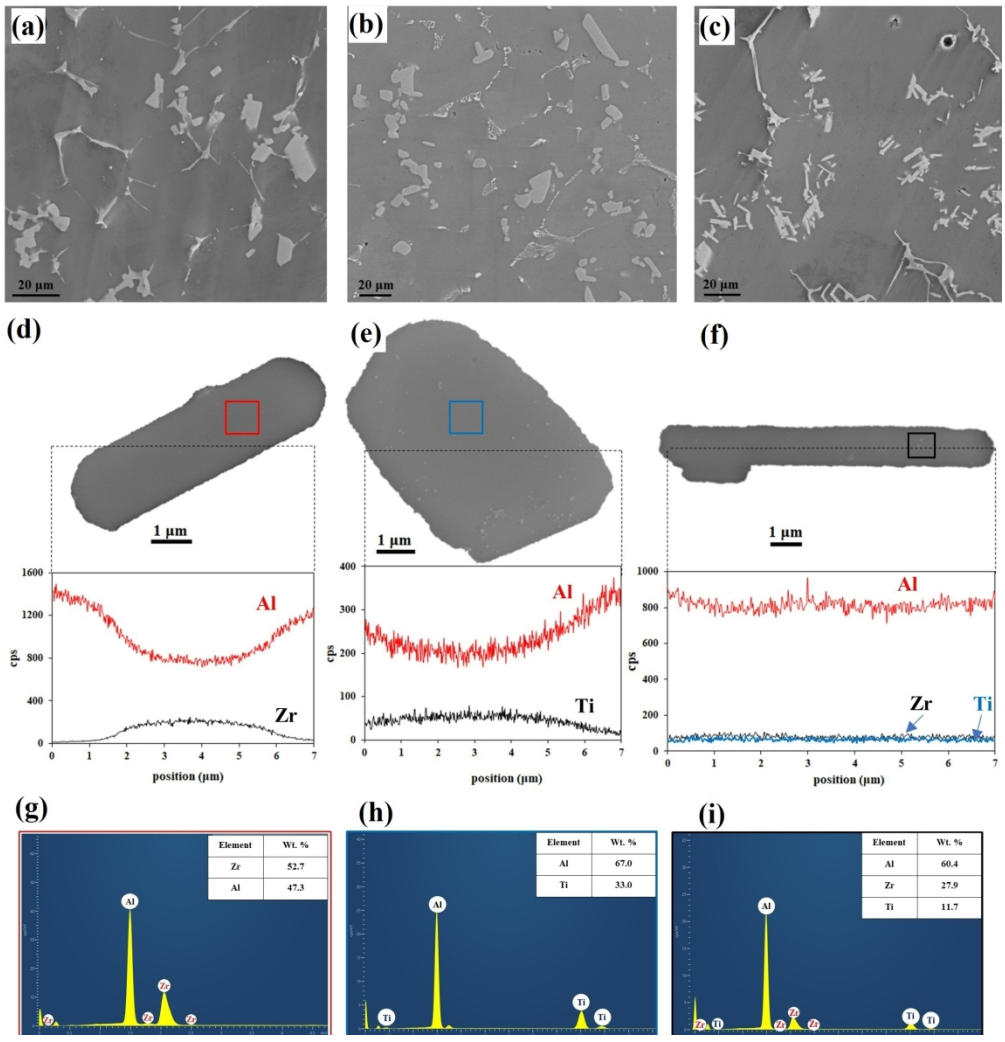

Fig. 2. Higher magnification secondary electron images of (a) Al_3Zr/Al, (b) Al_3Ti/Al, (c) hybrid *in situ* composites, (d-f) corresponding EDS line analysis images of the particles, and (g-i) corresponding EDS spectrum confirming the formation of the *in situ* particles respectively.

189x195mm (300 x 300 DPI)

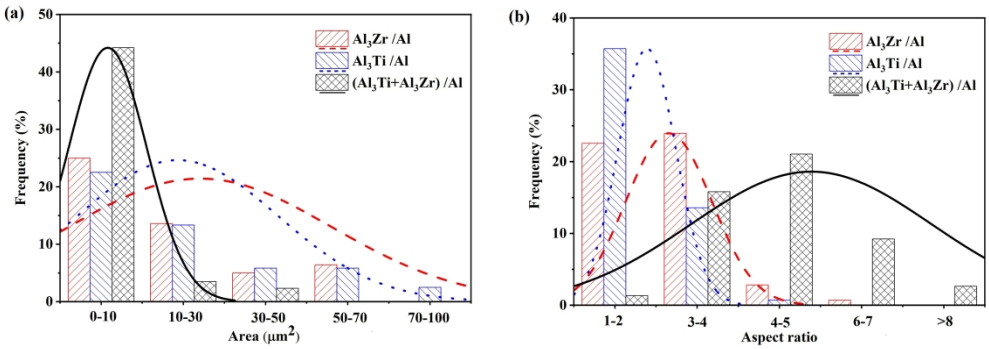

Fig. 3. Particle size distribution and corresponding normal fit of *in situ* formed (a) Al_3Zr, Al_3Ti, and Al_3Zr+Al_3Ti particles compared to the as-cast alloy in their respective composite, (b) Corresponding aspect ratio distribution of the particles.

313x113mm (300 x 300 DPI)

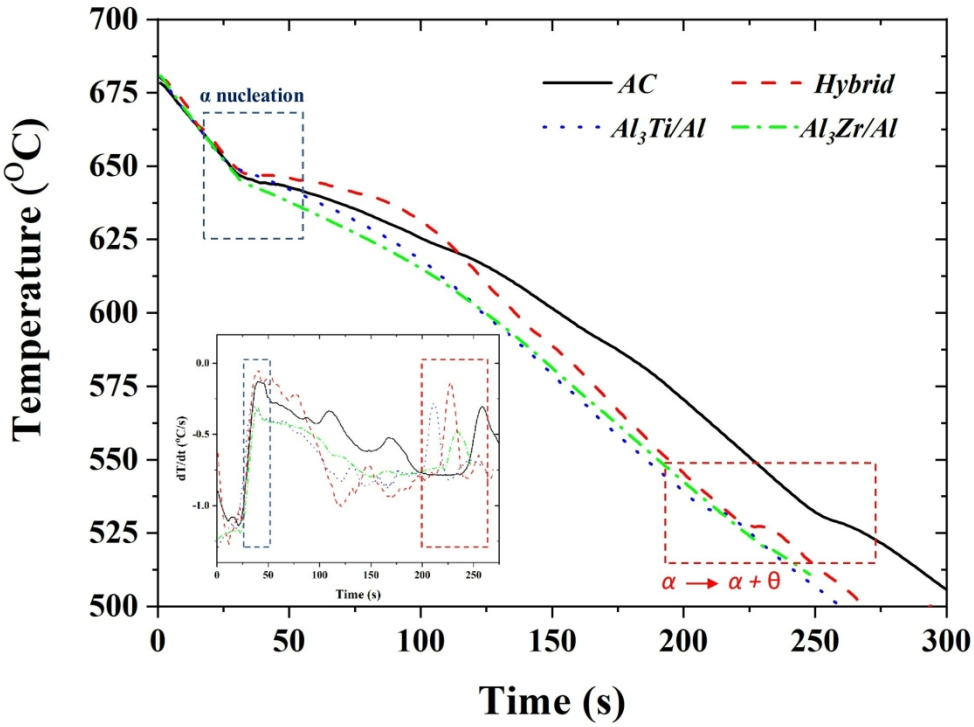

Fig. 4. Cooling curves of as-cast alloy and *in situ* composites. The inset shows the rate of the change of measured temperature of the melt, highlighting the first instance of solidification and eutectic temperature.

190x144mm (300 x 300 DPI)

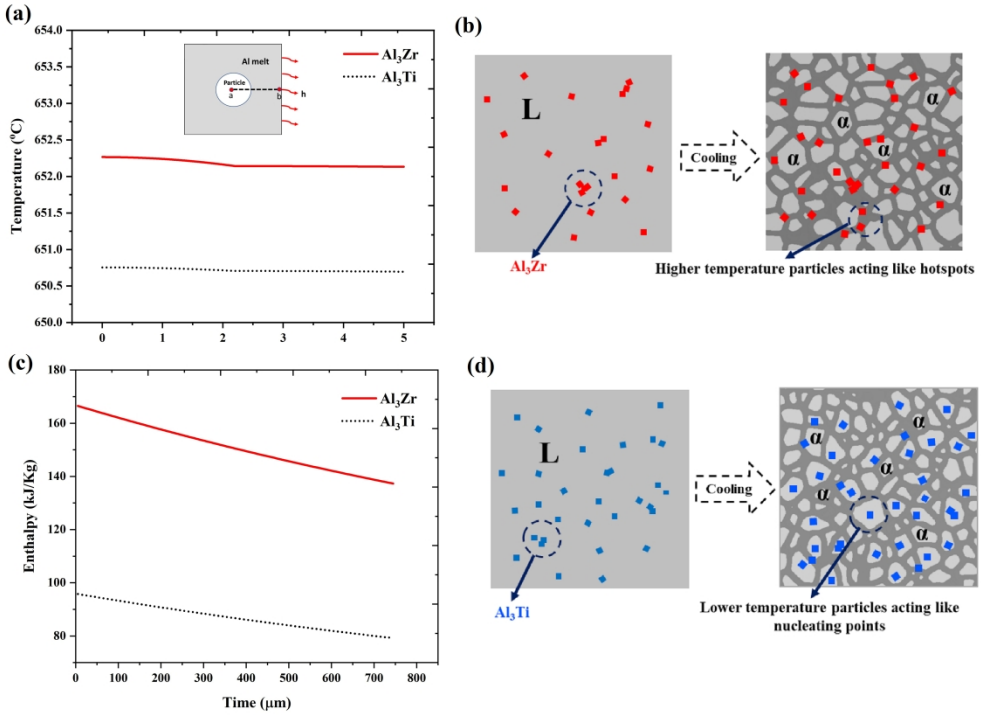

Fig. 5. (a) The variation of the temperature between the two types of particles, and the surrounding melt during solidification is shown in the inset and (c) The enthalpy variation at the interface between particle and the liquid metal for different particles with respect to time, (b) and (d) Schematic of nucleation mechanism of *in situ* Al_3Zr and Al_3Ti composites respectively.

355x264mm (300 x 300 DPI)

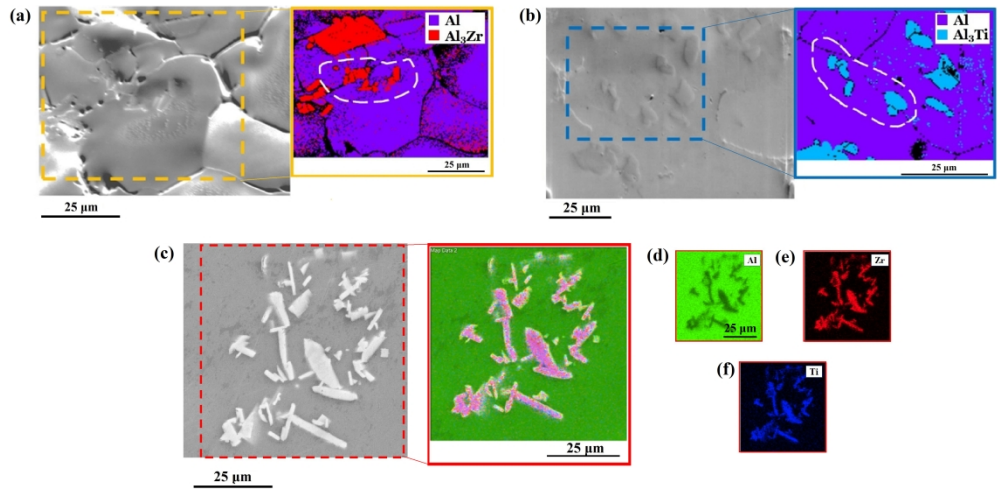

Fig. 6. Microstructure and EBSD phase distribution maps of (a). Al_3Zr/Al, (b). Al_3Ti/Al, and (c). Presence of Ti and Zr elements in EDS maps of hybrid composite, (d)-(f) EDS elemental mapping of aluminium, zirconium, and titanium respectively.

446x225mm (300 x 300 DPI)

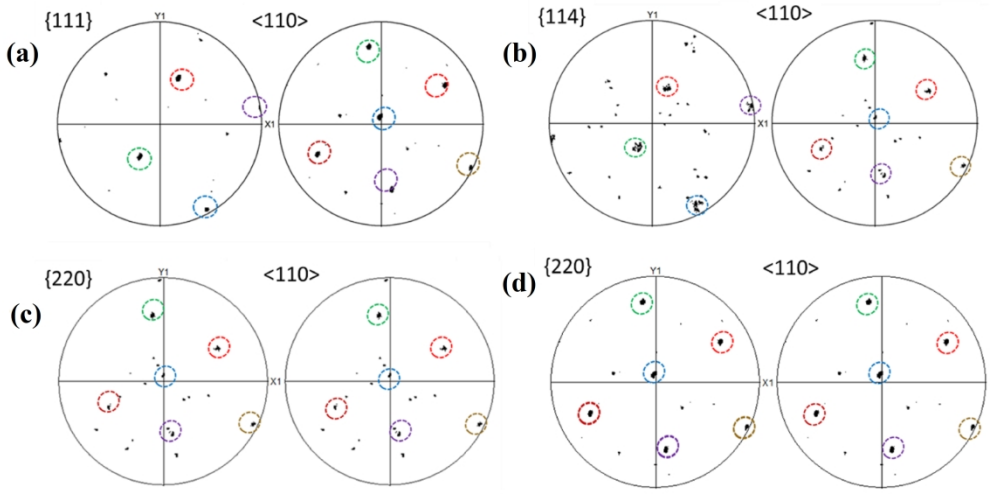

Fig. 7. Pole figures of *in situ* Al_3Zr/Al composites, (a) and (c) for α-Al phase, (b) and (d) for Al_3Zr phase (The dotted circles represent the pole dots of α-Al and Al_3Zr particles).

287x144mm (300 x 300 DPI)

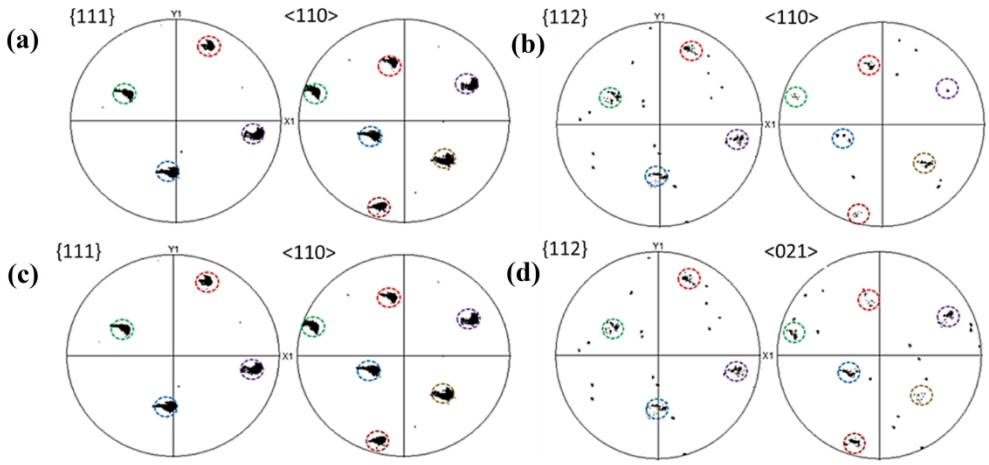

Fig. 8. Pole figures of *in situ* Al_3Ti/Al composites, (a) and (c) for α-Al phase, (b) and (d) for Al_3Ti phase (The dotted circles represent the pole dots of α-Al and Al_3Ti particles).

287x138mm (300 x 300 DPI)

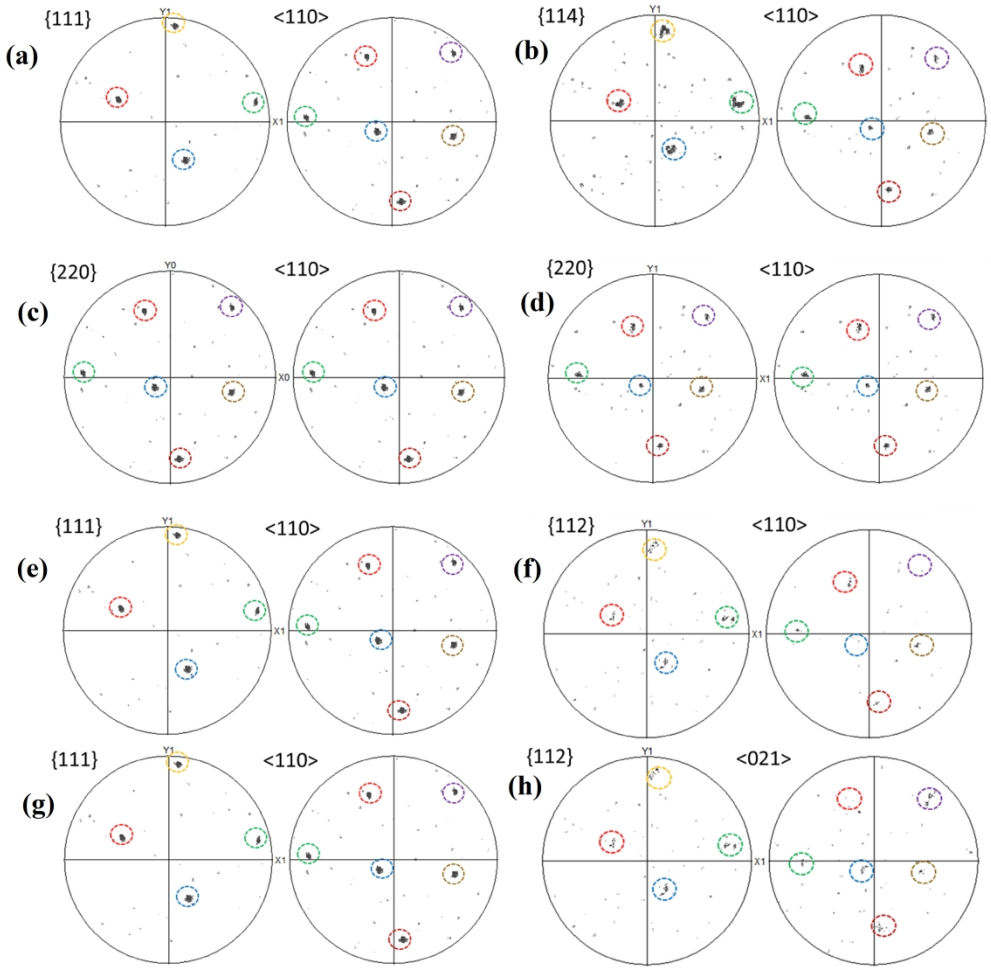

Fig. 9. Pole figures of *in situ* hybrid composite, (a), (c), (e), (g) for α-Al phase, (b) and (d) for Al_3Zr phase, (f) and (h) for Al_3Ti phase (The dotted circles represent the pole dots of α-Al, Al_3Zr and Al_3Ti particles).

287x283mm (300 x 300 DPI)

Table 1. Thermal parameters extracted from cooling curves (Fig. 4)

Samples	**Nucleation temperature (°C) (T_n)**	**Minimum temperature (°C) (T_m)**	**Undercooling (°C) $\Delta T = T_n - T_m$**
Al-5 wt.% Cu alloy	651.78	646.13	5.64
Al_3Zr/Al composite	647.99	644.21	3.77
Al_3Ti/Al composite	652.22	650.31	1.88
Hybrid *in situ* composite	648.8	647.91	0.93

For Peer Review

Table 2. E2EM model predicted crystallographic orientation relationships between Al, Al_3Ti and Al_3Zr particle

Material	a	b	c	Planes	f_d %	Directions	f_r %
Al	0.4049	-	-	-	-	-	-
Al_3Ti	0.3854	-	0.8584	$\{111\}_{Al}//\{112\}_{Al_3Ti}$	1.61	$<110>_{Al}//<021>_{Al_3Ti}$	0.73
				$\{111\}_{Al}//\{112\}_{Al_3Ti}$	1.61	$<110>_{Al}//<110>_{Al_3Ti}$	5.06
Al_3Zr	0.3999	-	1.7283	$\{111\}_{Al}//\{114\}_{Al_3Zr}$	1.18	$<110>_{Al}//<021>_{Al_3Zr}$	1.238
				$\{220\}_{Al}//\{220\}_{Al_3Zr}$	1.27	$<110>_{Al}//<220>_{Al_3Zr}$	1.238

For Peer Review

Supplementary Information

Role of *in situ* aluminide (Al_3Zr + Al_3Ti) particles on nucleation behavior of aluminium metal matrix composites

Merugu Rakesh[1], Neeraj Srivastava[1, +], Shishira Bhagavath[1, #] and Shyamprasad Karagadde[1, *]

[1]Department of Mechanical Engineering, Indian Institute of Technology Bombay, Mumbai 400076 India

[+] Current affiliation: Department of Mechanical Engineering, Sardar Vallabhbhai National Institute of Technology, Surat 395007 India

[#] Current affiliation: Department of Mechanical Engineering, University College London, WC1E 6BT, UK

*Corresponding author email: neeraj.s@med.svnit.ac.in, karagadde@iitb.ac.in

For Peer Review

Supplementary information 1:

To produce an Al-Cu alloy with a target composition of 5 wt. % Cu, a dilution process was used whereby pure aluminum was added to an Al-Cu alloy with a Cu content of 10 wt. %. The Al-Cu alloy ingot was melted in a coreless induction furnace. Pure aluminum wire pieces were then charged into the melt, and the mixture was stirred with a graphite stirrer for 30 minutes to ensure a homogeneous distribution of the added aluminum. The melt was then poured into a preheated steel mould. The solidified alloy was then extracted from the mould and further processed as required. The schematic of the experimental setup used in the study to fabricate *in situ* composites is shown in Fig. S1.

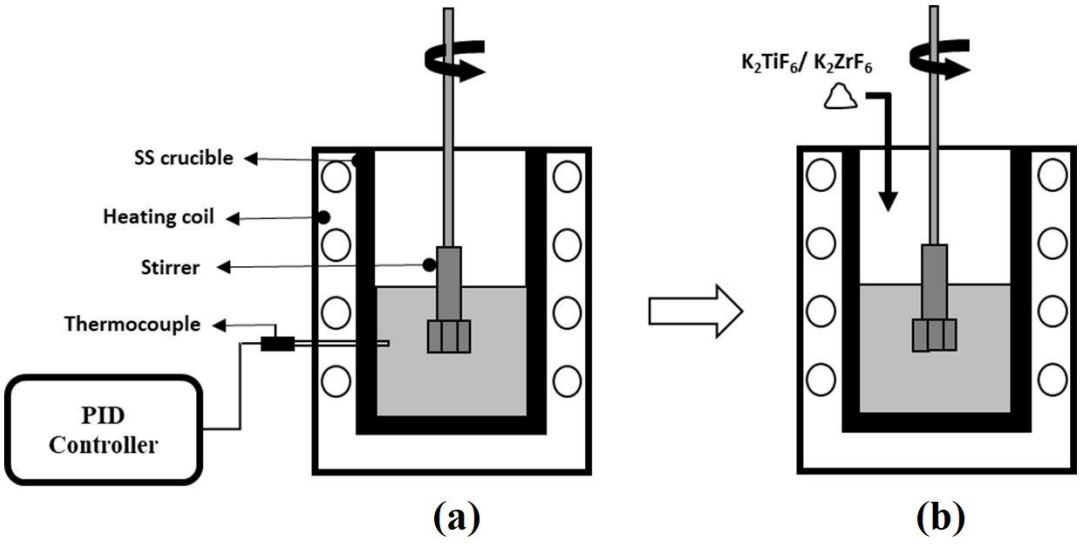

Figure S1: Schematic diagram of experimental setup for fabricating (a), as-cast samples and (b) *in situ* composites.

Supplementary information 2:

(Ref 1) reported the *in situ* reactions between the Al melt and K_2TiF_6 and K_2ZrF_6 to produce Al_3Ti and Al_3Zr respectively as follows,

$$3K_2TiF_6 + 13Al \rightarrow 3Al_3Ti + 2K_3AlF_6 + 2AlF_3 \qquad \Delta G = -122.8 \text{ kJ/mol} \qquad (1)$$

$$3K_2ZrF_6 + 13Al \rightarrow 3Al_3Zr + 2K_3AlF_6 + 2AlF_3 \qquad \Delta G = -31.8 \text{ kJ/mol} \qquad (2)$$

Supplementary information 3:

To understand the role of the specific heat of the particles heat conduction equation in polar coordinates is solved which is given by,

$$\frac{1}{r^2}\frac{\partial}{\partial r}\left(r^2\lambda\frac{\partial T}{\partial r}\right) + \frac{1}{r^2 sin^2\,\theta}\frac{\partial}{\partial\phi}\left(\lambda\frac{\partial T}{\partial\phi}\right) + \frac{1}{r^2 sin^2\,(\theta)}\frac{\partial}{\partial\theta}\left(\lambda sin\,(\theta)\frac{\partial T}{\partial\theta}\right) = \rho c\frac{\partial T}{\partial t} \qquad (3)$$

Where, T, r, t is temperature (Kelvin), radius (meters) and time (seconds) respectively. θ and ϕ are polar and azimuthal angle. λ_i, ρ_i, c_i are the thermal conductivity (W/m-K), density (kg/m^3) and specific heat (J/kg-K) at cell 'i'. For spherically axi-symmetric case (no dependence on ϕ, θ)

$$\frac{1}{r^2}\frac{\partial}{\partial r}\left(r^2\lambda\frac{\partial T}{\partial r}\right) = \rho c\frac{\partial T}{\partial t} \qquad (4)$$

$$\frac{\partial}{\partial r}\left(\lambda\frac{\partial T}{\partial r}\right) + \frac{2\lambda}{r}\left(\frac{\partial T}{\partial r}\right) = \rho c\frac{\partial T}{\partial t} \qquad (5)$$

By using central differences formulations, we obtain the following final equation,

$$T_i^{t+1} = T_i^t + \frac{\Delta t}{\rho_i c_i}\left\{\left(\frac{\lambda_i}{r\Delta r}(T_{i+1} - T_{i-1})\right) + \frac{1}{(\Delta r)^2}\left(\frac{2\lambda_i\lambda_{i+1}}{\lambda_i + \lambda_{i+1}}(T_{i+1} - T_{i-1}) - \frac{2\lambda_i\lambda_{i-1}}{\lambda_i + \lambda_{i-1}}(T_{i+1} - T_{i-1})\right)\right\} \qquad (6)$$

The problem is solved by taking following boundary conditions,

At $r = 0$, due to axis-symmetry, we have $\frac{\partial T}{\partial r} = 0$, and

At $r = R$, we assume convection. So, we have

$$\left(-\lambda\frac{\partial T}{\partial r}\right) = h(T - T_\infty) \qquad (7)$$

For Peer Review

(Ref 2) experimented with the solidfication of Aluminium metal in graphite crucible and found the value of (*h)* heat transfer coefficient (4700 W/m^2-K) of the melt. T_∞ is surrounding temperature.

On discretizing and rearranging (Eq. 5) we get,

$T_0 = T_1$ at $r = 0$, and,

$$T_{N-1} = \frac{\lambda_{eff} T_{N-2} + h\Delta r T_\infty}{\lambda_{eff} + h\Delta r}, \text{ at r=R} \quad (8)$$

Where (λ_{eff}) effective thermal conductivity is given as,

$$\lambda_{eff} = \frac{2\lambda_{N-1}\lambda_{N-2}}{\lambda_{N-1} + \lambda_{N-2}} \quad (9)$$

The finite different equation was solved in MATLAB R2020b. Grid independence test was performed and a grid size of 3000 was found to be suitable. Thermal properties of the particles were reported by (Ref 3)) for Al_3Ti particles and (Ref 4)) for Al_3Zr particles as shown in Table S1.

Table S1: Thermal properties used in the numerical analysis.

Property	Al	Al_3Zr	Al_3Ti
Specific Heat, C_P (kJ/kg-K)	923	163	93.75
Density, ρ (kg/m^3)	2720	4110	3400
Thermal Conductivity, λ (W/m-K)	237	1.02	1.22

For Peer Review

References

1. I. Dinaharan, G. Ashok Kumar, S.J. Vijay, and N. Murugan, Development of Al3Ti and Al3Zr Intermetallic Particulate Reinforced Aluminum Alloy AA6061 in Situ Composites Using Friction Stir Processing, *Mater Des*, Elsevier Ltd, 2014, **63**, p 213–222.

2. V.E. Bazhenov, A. V. Koltygin, Y. V. Tselovalnik, and A. V. Sannikov, Determination of Interface Heat Transfer Coefficient between Aluminum Casting and Graphite Mold, *Russian Journal of Non-Ferrous Metals*, 2017, **58**(2), p 114–123.

3. Y.H. Duan, Y. Sun, and L. Lu, Thermodynamic Properties and Thermal Conductivities of TiAl 3-Type Intermetallics in Al-Pt-Ti System, *Computational Materials Science*, 2013, **68**, p 229–233.

4. D.L. Li, P. Chen, J.X. Yi, B.Y. Tang, L.M. Peng, and W.J. Ding, Thermal Properties of the FCC Al3Zr: First-Principles Study, *Materials Science Forum*, 2010, **650**, p 313–319.

Figure captions:

Figure S1: Schematic diagram of experimental setup for fabricating (a), as-cast samples and (b) *in situ* composites.

For Peer Review

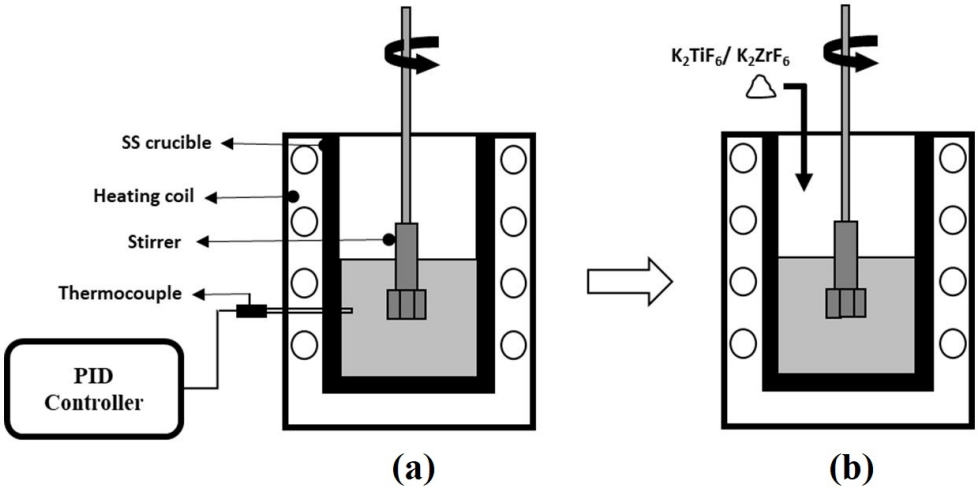

Figure S1: Schematic diagram of experimental setup for fabricating (a), as-cast samples and (b) *in situ* composites.

107x58mm (300 x 300 DPI)

Table S1. Thermal properties used in the numerical analysis.

Property	Al	Al_3Zr	Al_3Ti
Specific Heat, C_P (kJ/Kg-K)	923	163	93.75
Density, ρ (Kg/m^3)	2720	4110	3400
Thermal Conductivity, λ (W/m-K)	237	1.02	1.22

For Peer Review